

---

Faculty of Science

Faculty Publications

---

This is a post-print version of the following article:

Structure dependency of the atomic-scale mechanisms of platinum electro-oxidation and dissolution

Timo Fuchs, Jakub Drnec, Federico Calle-Vallejo, Natalie Stubb, Daniel J. S. Sandbeck, David A. Harrington, ... & Olaf M. Magnussen

August 2020

The final publication is available at:

<https://doi.org/10.1038/s41929-020-0497-y>

---

Citation for this paper:

Fuchs, T., Drnec, J., Calle-Vallejo, F., Stubb, N., Sandbeck, D. J. S., Harrington, D. A., ... Magnussen, O. M. (2020). Structure dependency of the atomic-scale mechanisms of platinum electro-oxidation and dissolution. *Nature Catalysis*, 3, 754-761. <https://doi.org/10.1038/s41929-020-0497-y>.

# Structure-dependence of the atomic-scale mechanisms of Pt electrooxidation and dissolution

Timo Fuchs<sup>1</sup>, Jakub Drnec<sup>2</sup>, Federico Calle-Vallejo<sup>3</sup>, Natalie Stubb<sup>4</sup>,  
Daniel J. S. Sandbeck<sup>5,6</sup>, Martin Ruge<sup>1</sup>, Serhiy Cherevko<sup>5</sup>,  
David A. Harrington<sup>4</sup> & Olaf M. Magnussen<sup>1\*</sup>

July 13, 2020

1. Institut für Experimentelle und Angewandte Physik, Christian-Albrechts-Universität zu Kiel, Olshausenstr. 40, 24098 Kiel, Germany
2. Experimental division, European Synchrotron Radiation Facility, 71 Avenue des Martyrs, 38000 Grenoble, France
3. Departament de Ciència de Materials i Química Física & Institut de Química Teòrica i Computacional (IQTCUB), Universitat de Barcelona, Martí i Franquès 1, 08028 Barcelona, Spain.
4. Chemistry Department, University of Victoria, Victoria, British Columbia, V8W 2Y2, Canada
5. Helmholtz-Institute Erlangen-Nürnberg for Renewable Energy (IEK-11), Forschungszentrum Jülich GmbH, 91058 Erlangen, Germany
6. Department of Chemical and Biological Engineering, Friedrich-Alexander-Universität Erlangen-Nürnberg, 91058 Erlangen, Germany

\* Corresponding author

## Abstract

Platinum dissolution and restructuring due to surface oxidation are primary degradation mechanisms that limit the lifetime of Pt-based electrocatalysts for electrochemical energy conversion. Here, we studied well-defined Pt(100) and Pt(111) electrode surfaces by in situ high-energy surface X-ray diffraction, on-line inductively coupled plasma mass spectrometry, and density functional theory calculations, to elucidate the atomic-scale mechanisms of these processes. The locations of the extracted Pt atoms after Pt(100) oxidation reveal distinct differences from the Pt(111) case, which explains the different surface stability. The evolution of a specific stripe oxide structure on Pt(100) produces unstable surface atoms which are prone to dissolution and restructuring, leading to one order of magnitude higher dissolution rates.

## Introduction

The degradation of Pt catalysts for the cathode reaction in fuel cells is linked to their electrooxidation and dissolution.<sup>1</sup> Both these processes are arguably even more complex than the actual energy conversion via oxygen reduction and have been studied for a long time, mainly on polycrystalline and supported nanoparticle catalysts. Single-crystal studies offer the prospect of a more detailed understanding of these processes at the atomic level.<sup>2–11</sup> Some such studies followed these processes with potential cycling, where it is known that the surface restructuring over many cycles leads to a roughened surface, and that dissolution is enhanced during oxide reduction.<sup>12–22</sup> Explanation of this behaviour generally invokes a place exchange (PE) process, in which a Pt surface atom leaves its lattice site and oxygen penetrates into the metal lattice. On Pt(111), pioneering studies demonstrated that PE can be directly observed by surface X-ray diffraction (SXRD).<sup>4,5</sup> More recent SXRD measurements confirmed this<sup>18,23–25</sup> and allowed structural refinement, showing that the exchanged Pt atom lies 2.4 Å above its original lattice site,<sup>18</sup> in good agreement with density functional theory (DFT) studies of this process.<sup>26–28</sup> In contrast to Pt(111), other Pt crystal faces show distinct differences in the oxidation and dissolution behaviour.<sup>10,12,14,29</sup> This has been qualitatively explained by the more open arrangement of the surface atoms, but precise atomic level data are scarce. Thus, clear structure-reactivity relationships, which e.g. would guide the development of tailored Pt catalysts, are still lacking.

We here present detailed structural studies, focussing on the precise atomic motions in these early stages of oxidation. By correlating *in situ* SXRD measurements, which reveal how the place-exchanged Pt atoms are arranged in the initial stages of surface oxidation, with detailed DFT studies of this process, a direct comparison of the elementary processes underlying Pt(111) and Pt(100) oxidation becomes possible. Our study reveals a sharply different mechanism for the oxidative extraction of Pt atoms out of the two surfaces, providing a detailed explanation for the enhanced dissolution on Pt(100), observed by on-line mass spectroscopy.

## 45 Results

### 46 Dissolution and surface restructuring by electrooxidation.

47 According to cyclic voltammetry (CV) studies, the onset of Pt oxidation is  
48 marked on these two surfaces by a current peak above 1.0 V (labelled  $O_{ads}$  in  
49 Fig. 1b, c and Extended Data Fig. 1). However, the CV of Pt(100) irreversibly  
50 changes in subsequent cycles, whereas that of Pt(111) remains stable for an up-  
51 per potential limit (UPL) of  $\lesssim 1.15$  V and thus can be mistaken for an oxidation  
52 process without surface restructuring.<sup>7, 12, 29</sup>

53 The (ir)reversibility of the CVs is mirrored in the Pt dissolution rates obtained  
54 by inductively coupled plasma mass spectrometry (ICP-MS) in a (capillary)  
55 scanning flow cell (CSFC and SFC) with results summarised in Fig. 1a,d. The  
56 facet dependent trends are readily apparent. At sweep rates of  $\gtrsim 10$  mV/s, no  
57 dissolution is seen for either surface for CVs with an UPL of 1.0 V, in agreement  
58 with previous results.<sup>14, 16</sup> When increasing the UPL, the onset of significant  
59 anodic dissolution due to Pt oxidation is observed for Pt(100) as soon as the  
60  $O_{ads}$  peak begins, while for Pt(111) the onset only occurs at potentials above 1.2  
61 V. Cathodic dissolution during the oxide reduction is observed for both surfaces  
62 at UPLs  $\geq 1.1$  V; however, the dissolution of Pt(100) exceeds that of Pt(111) by  
63 about one order of magnitude. The onset and amount of dissolution depends on  
64 the precise time-potential program, reflecting the slow oxidation kinetics,<sup>14</sup> but  
65 the enhanced rates for Pt(100) as compared to Pt(111) are found in all experi-  
66 ments. It is noted that the amount of oxide formed in both cases is comparable,  
67 only about 20% higher for Pt(100) (as seen from the integral of the oxidation  
68 peaks in the CVs). Thus, the significant difference in dissolution rates points  
69 towards a fundamentally different oxidation behaviour of the two surfaces. Sim-  
70 ilar facet dependent trends have been found in previous comparative studies of  
71 the dissolution behaviour of Pt(100) and Pt(111),<sup>14, 16</sup> but these do not link the  
72 difference to the oxide structure and also do not provide mechanistic explana-  
73 tions, due to the lack of knowledge on the structural changes during surface  
74 oxidation.

75 The atomic scale origin of this difference was investigated by *in situ* surface  
76 X-ray diffraction (SXRD). This technique determines the exact positions of sur-  
77 face atoms during the initial stages of oxidation, which can then be linked to the  
78 dissolution and surface restructuring mechanisms. For a qualitative assessment  
79 of the influence of surface orientation, we first followed reflections near the anti-  
80 Bragg positions of the crystal truncation rods (CTRs). Those are sensitive to  
81 the distortion of the ideal Pt lattice and the extraction of Pt atoms out of the  
82 surface in the place exchange process.<sup>4, 5, 23</sup> Performing such measurements dur-  
83 ing potential cycles revealed that on both surfaces the onset of PE coincides with  
84 the  $O_{ads}$  peak maximum (0.98 V and 1.04 V on Pt(100) and Pt(111), respec-  
85 tively), but that the subsequent structural response is very different (Fig. 1b,c).  
86 PE on Pt(100) results in irreversible surface structural changes, as indicated  
87 by the irreversible decrease in X-ray intensity after completion of one potential  
88 cycle. In contrast, the PE process on Pt(111) is initially fully reversible<sup>4, 23</sup>

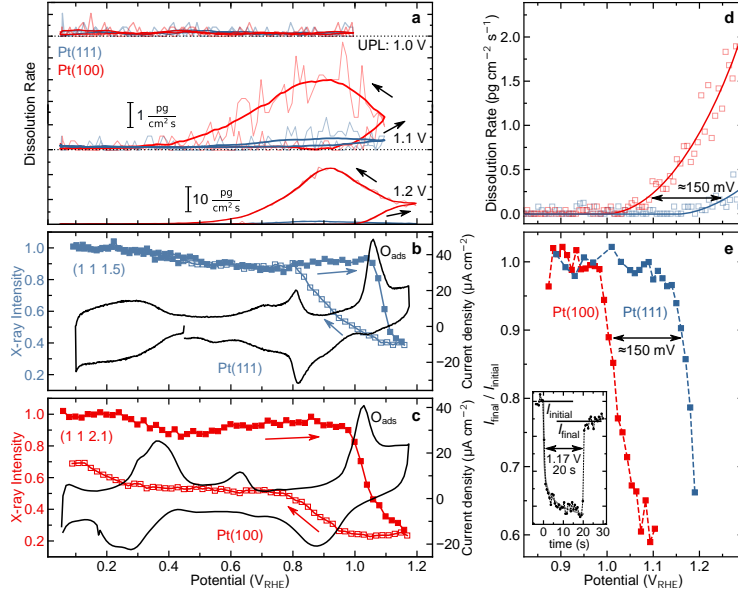


**Fig. 1. Dissolution and atomic-scale structural changes during Pt oxidation.** (a) Pt dissolution during cycles at 50 mV/s to increasingly positive potential limits (UPL) obtained using the capillary scanning flow cell, illustrating that the cathodic dissolution during oxide reduction is significantly more pronounced on Pt(100). X-ray intensity changes at the anti-Bragg positions of selected crystal truncation rods and simultaneously measured cyclic voltammograms of (b) Pt(111) (data taken from Ref. 23) and (c) Pt(100) during potential cycles at 20 mV/s. Pt place exchange (PE), indicated by the intensity drop at the  $O_{ads}$  peak, is initially fully reversible on Pt(111), whereas for Pt(100) it always results in irreversible surface restructuring. (d) Potential-dependent Pt dissolution rates during a positive sweep at 10 mV/s obtained with the scanning flow cell, showing the onset of anodic dissolution. (e) Reversibility of the PE process, determined by potential step experiments, where the potential was changed for 20 s from 0.47 V in the double layer range to a potential in the oxidation regime and then moved back to 0.47 V (illustrated in inset). The relative changes in X-ray intensity indicate that irreversible Pt surface restructuring starts at  $\approx 150$  mV higher potentials on Pt(111) than on Pt(100).

and only results in irreversible surface restructuring if the upper potential limit exceeds 1.15 V. Here, the onset of irreversibility occurs above a critical coverage of extracted Pt atoms,<sup>23</sup> which depends on potential and time in the oxidation regime. A more quantitative comparison of the onset of irreversible intensity changes, obtained in potential step experiments (Fig. 1e), indicates that these occur on Pt(111) at about 150 mV more positive potentials than on Pt(100), closely mirroring the onset of Pt dissolution (Fig. 1d). This unambiguously demonstrates that on single crystal surfaces dissolution and irreversible surface structural changes are linked.

Although the latter was already stated in the work of Lopes et al.,<sup>14,15</sup> here the dissolution behaviour was attributed to irreversible Pt oxide formation at the peak around 1 V, where on Pt(111) oxidation is still largely reversible. Furthermore, our observations resemble the *in situ* Raman spectroscopy data by Huang et al.,<sup>10</sup> who reported that bands associated with the formation of 3D  $\alpha$ -PtO<sub>2</sub> oxide phase occur at 200 mV more negative potentials on Pt(100) than on Pt(111). However, PE on Pt(111) was here proposed to occur only at  $\geq 1.3$  V, which is at variance with the SXRD results. Therefore, a clear correlation between the precise oxide structure of different Pt surfaces, its reversibility, and its effect on the dissolution is still lacking.

## Atomic-scale structure of the Pt oxide.

To assess the difference between the reversible and irreversible structural processes, we performed a detailed potential-dependent surface crystallographic analysis of an extended set of CTRs. An overview of all measured data sets is given in Supplementary Note 1. For Pt(111) the surface atom arrangement was determined in our previous study.<sup>18,23</sup> At low coverage, the PE was found to result only in an  $\approx 2$  Å vertical displacement of the extracted Pt atom (Pt<sub>ex</sub>), whereas the in-plane position remains the same. The Pt<sub>ex</sub> thus is located directly above its original site, which is now vacated or filled with oxygen. Previous density functional theory (DFT) studies also found this unusual geometry and indicated that it is stabilised by three neighbouring oxygen adsorbates on the Pt(111) surface.<sup>27</sup>

Similar structural characterisation of the initial stages of Pt(100) oxidation is more difficult, because unlike on Pt(111), the surface oxide continuously evolves over time scales of hours. This strongly impedes conventional SXRD measurements, which typically require 1 - 2 h recording time. We therefore performed *in situ* measurements by the novel technique of high-energy surface X-ray diffraction (HESXRD),<sup>30</sup> which allows collection of many CTRs in just a few minutes, i.e. in a time period over which the structural changes in the oxide are negligible. Examples of the CTRs measured on Pt(100) are shown in Fig. 2a (see Extended Data Fig. 3 for the full data set). Measurements at 0.12 V (Extended Data Fig. 2 and Supplementary Figure 2) confirm that the initial surface is unreconstructed and exhibits negligible roughness. At potentials slightly negative of the O<sub>ads</sub> peak in the CV, adsorption of oxygen species is signalled by changes in the Pt surface relaxation and increased statistical deviations of Pt

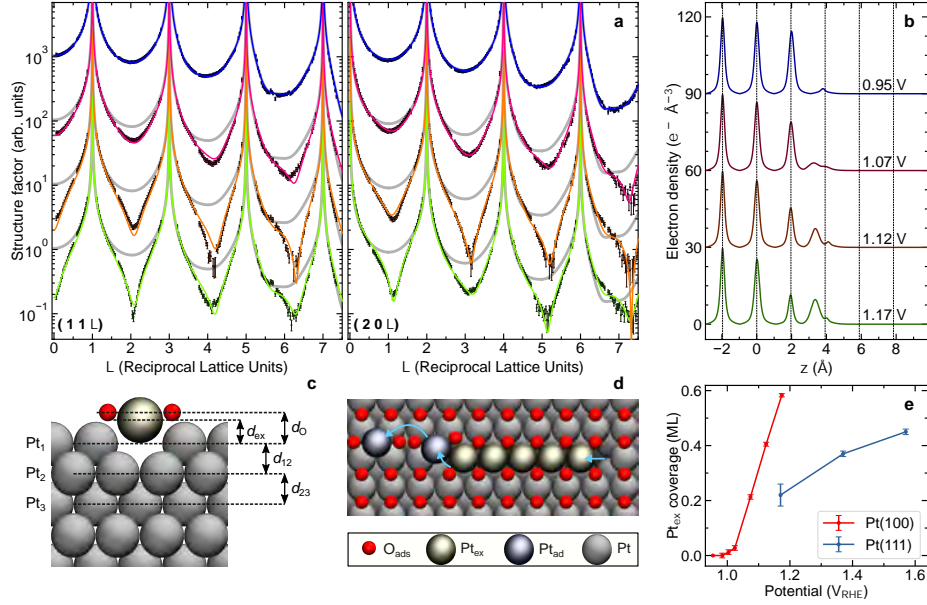


**Fig. 2. Atomic structure of the place exchange site on Pt(100).** (a) Two of the 11 measured crystal truncation rods (CTR) of Pt(100), obtained by *in situ* high energy surface x-ray diffraction measurements (68 keV) at a potential slightly negative (0.95 V) and three potentials positive (1.07, 1.12 and 1.17 V) of the  $\text{O}_{\text{ads}}$  peak in the cyclic voltammogram (Fig. 1b, Extended Data Fig. 1). The latter exhibit significantly decreased intensities and correspond to surfaces in which 20 to 60 % of the Pt atoms underwent place exchange. Each set of CTRs was recorded within 550 s, starting 300 s after the potential was established. The full CTR sets are given in Extended Data Fig. 3. In addition to the experimental data, which are offset by a factor of 10 with respect to each other, the best fit (coloured lines) and the CTR fits for the smooth surface at 0.95 V (grey line) are shown. (b) Electron density profile along the surface normal, obtained from the quantitative modelling of the CTRs. The bulk Pt lattice positions are indicated by dashed vertical lines. (c) Side and (d) top view of the atomic arrangement of the extracted Pt atoms (the labels correspond to the parameters in Supplementary Table 2). (e) Potential-dependent  $\text{Pt}_{\text{ex}}$  coverage on Pt(100), obtained from the crystal truncation rod analysis, compared with the  $\text{Pt}_{\text{ex}}$  coverage on Pt(111) (taken from Ref. 18).

surface atoms from ideal lattice positions, characterised by larger Debye-Waller factors. After the onset of PE, the intensity of all CTRs substantially decreases. This change cannot be described by  $\text{Pt}_{ex}$  in an on-top geometry, as in the case of Pt(111), or in conventional hollow or bridge sites atop the Pt surface. (see Supplementary Note 3 for details on the data analysis). A good description of the large HESXRD data sets was only possible by models that assume that the majority of extracted Pt atoms reside in bridge sites with vertical positions that are merely 1.40 Å ( $d_{ex}$  in Fig. 2c) above the Pt(100) surface plane (Fig. 2b). These models allowed fitting all of the CTR data obtained at different oxidation potentials, with very similar structure parameters, apart from the  $\text{Pt}_{ex}$  coverage, which continuously increased up to 0.6 ML with increasing potential (Fig. 2e, see Supplementary Table 2 for all structural parameters). It is noted that on Pt(111) the  $\text{Pt}_{ex}$  coverage increases more moderately, to 0.45 ML at 1.57 V.<sup>18</sup> The low vertical position of the  $\text{Pt}_{ex}$  is sterically incompatible with species residing atop the surface, but can be readily explained by Pt atoms that are bound via surface or subsurface oxygen to the centre of a vacancy dimer. The resulting geometry distinctly differs from that of  $\text{Pt}_{ex}$  on Pt(111), both in terms of the coordination as well as the distances of the  $\text{Pt}_{ex}$  to the neighbouring atoms in the Pt surface layer (about 0.2 Å larger) and the vertical spacing of the  $\text{Pt}_{ex}$  atoms from the layer below ( $d_{ex} > 2.23$  Å<sup>18</sup> on Pt(111),  $d_{ex} < 1.42$  Å on Pt(100)). Formation of such a vacancy dimer requires extraction of a second Pt atom from the surface layer ( $\text{Pt}_{ad}$ ), which can be positioned as an adatom on the neighbouring Pt surface or as a slightly more protruded atom on the end of the dimer. However,  $\text{Pt}_{ex}$  and  $\text{Pt}_{ad}$  are not necessarily generated in equal numbers. For example, only one additional  $\text{Pt}_{ad}$  would be produced in the growth of a Pt oxide chain structure (Fig. 2d), similar to those found in scanning tunneling microscopy studies<sup>31,32</sup> and density functional theory (DFT) calculations<sup>26</sup> of Pt(111) oxidation in the gas-phase. In this case, the  $\text{Pt}_{ad}$  would only be formed as a minority species, not necessarily detectable in SXRD experiments. Indirect support for this scenario comes from CTR data obtained at 0.12 V after oxide reduction, which is shown in Extended Data Fig. 2. Here,  $\text{Pt}_{ad}$  in hollow sites are clearly present, but at coverages that are ten times lower than that of the  $\text{Pt}_{ex}$  in the corresponding oxide film. This suggests that also on Pt(100) the majority of  $\text{Pt}_{ex}$  directly return into surface vacancies after reduction.

## Mechanism of oxide formation and Pt dissolution.

To further confirm the proposed structural development, we performed a comparative DFT study of the PE and Pt dissolution processes. We first calculated the Pourbaix diagrams for Pt(111) and Pt(100) (Extended Data Fig. 5) to determine the most stable oxygen coverage and adsorption sites as a function of pH and applied potential. The stabilization granted by water wetting was taken into account in the free energy assessment of all species (see the Methods section for further details).

In good agreement with the experimental data (Fig. 1b,c), platinum extraction is calculated to be thermodynamically favourable starting from 1.06 V at  $\theta_{\text{O}}$



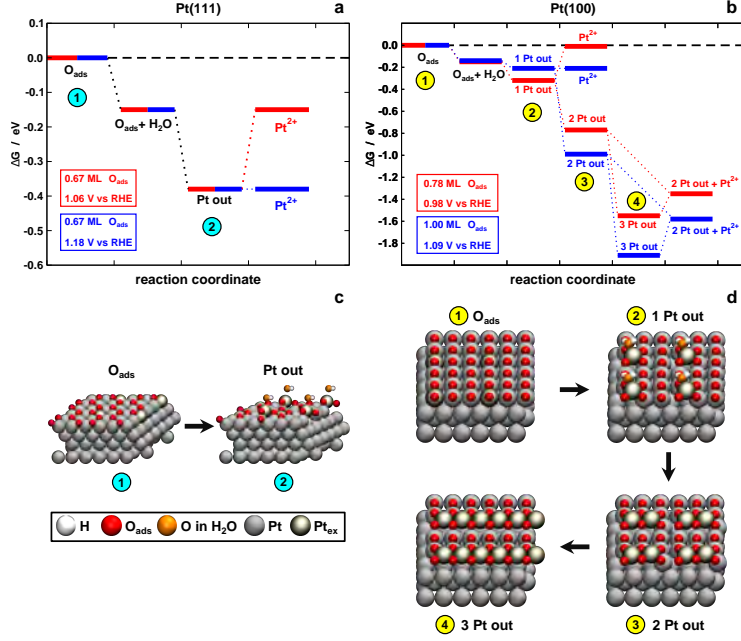


**Fig. 3. Atomistic view of place exchange and dissolution on Pt(111) and Pt(100).** Free energy landscapes of place exchange and dissolution obtained by density functional theory calculations of (a) Pt(111) and (b) Pt(100). Corresponding schematics of the main steps in the reaction pathway are shown in (c) and (d) for Pt(111) and Pt(100), respectively. In both cases, surface wetting by  $\text{H}_2\text{O}$  is accounted for and observed to aid the extraction process (for clarity,  $\text{H}_2\text{O}$  is not shown in step (3) and (4) of (d)). Dissolution of the first  $\text{Pt}_{\text{ex}}$  in form of  $\text{Pt}^{2+}$  is not favoured at low potentials (1.06 V on Pt(111), 0.98 V on Pt(100)), but becomes energetically favourable at higher potentials (1.18 V on Pt(111), 1.09 V on Pt(100)). Further Pt extraction proceeds differently on Pt(100), where a second and third extraction is favourable, leading to an extended extracted stripe of Pt atoms. Parallel to the stripe extraction process, dissolution can already occur at 0.98 V through detachment of one of Pt atoms in the dimer formed after the second stripe extraction. Top and side views of the surfaces are provided in Extended Data Fig. 6.

177  $\approx 0.67$  ML on Pt(111) and  $\geq 0.98$  V at  $\theta_{\text{O}} \approx 0.78$  ML for Pt(100) (Extended  
 178 Data Fig. 4). According to energy calculations of the various steps in the PE  
 179 process (Fig. 3a,b), PE starts on Pt(111) with  $\text{O}_{\text{ads}}$  adsorption (Fig. 3, step  
 180 (1)) followed by the extraction of a Pt atom (step (2)). In line with previous  
 181 SXRD<sup>18,23</sup> and DFT<sup>27</sup> studies, the extracted Pt atom is located above a va-  
 182 cancy, and is coordinated to three  $\text{O}_{\text{ads}}$  atoms (Fig. 3c, Extended Data Fig. 6).  
 183 Our extraction pathway on Pt(111) is similar to the one reported by Eslamibid-  
 184 goli and Eikerling,<sup>27</sup> who found that PE starts at oxygen coverages between 0.59  
 185 and 0.75 ML. The pathway for PE on Pt(100) is substantially different from that  
 186 on Pt(111) (Fig. 3b). Although it also starts by  $\text{O}_{\text{ads}}$  adsorption and the extrac-  
 187 tion of a Pt atom, the high  $\text{O}_{\text{ads}}$  coverage allows Pt extraction to immediately  
 188 proceed at neighbouring sites. Hence, there is a consecutive extraction of Pt  
 189 atoms that ultimately leads to the creation of a stripe of protruded atoms. In  
 190 agreement with our experiments, the  $\text{Pt}_{\text{ex}}$  are not located above their original  
 191 lattice sites but move sideways to a square-planar site where they are coordi-  
 192 nated to four  $\text{O}_{\text{ads}}$  atoms. Because of the latter, this arrangement is strongly  
 193 stabilised, contrary to Pt(111), where stripe-like structures only lead to small  
 194 gains in free energy as compared to isolated  $\text{Pt}_{\text{ex}}$ .<sup>26</sup> The larger  $\text{O}_{\text{ads}}$  coordi-  
 195 nation around the  $\text{Pt}_{\text{ex}}$  may lead to the Raman signature resembling  $\text{PtO}_2$ , as  
 196 observed for Pt(100) in this potential range.<sup>10</sup> Furthermore, we note that the  
 197 first  $\text{Pt}_{\text{ex}}$  of each stripe has to deviate from the perfect square-planar site for  
 198 steric reasons (see  $\text{Pt}_{\text{ex}}$  positions after first and second extraction), resulting in  
 199 the more weakly bound  $\text{Pt}_{\text{ad}}$  species postulated above.  
 200 The differences in Pt(111) and Pt(100) anodic dissolution upon oxidation, i.e.  
 201 the conversion of  $\text{Pt}_{\text{ex}}$  to a Pt ion (assumed to be  $\text{Pt}^{2+}$ ),<sup>33</sup> can be ascribed to  
 202 the different Pt extraction process. On Pt(111), the  $\text{Pt}_{\text{ex}}$  are initially arranged  
 203 directly above the vacancy and this is thermodynamically more stable than a  
 204  $\text{Pt}^{2+}$ -vacancy pair (Fig. 3a and note in the Methods section). Only after the po-  
 205 tential increases to 1.18 V does the dissolution become energetically favourable  
 206 (Fig. 3a and Extended Data Fig. 4). The situation is different on Pt(100) (Fig.  
 207 3b), where the dissolution is not favoured at 0.98 V during the first extraction,  
 208 but the atomic arrangement formed after the second extraction is prone to dis-  
 209 solution. DFT calculations show this process to be exothermic and to result  
 210 in the same structure after removal of a  $\text{Pt}_{\text{ex}}$  atom from the second and third  
 211 extraction state. The reason for this is that in the case of dissolution from  
 212 the second extraction state subsequent extraction of a further Pt surface atom  
 213 occurs. This leads to stabilization of the system, because the formed dimer is  
 214 now better positioned in the triple vacancy. Thus, the  $\text{Pt}_{\text{ex}}$  atoms formed in the  
 215 initial stages of stripe formation as well as the more weakly bound  $\text{Pt}_{\text{ad}}$  at the  
 216 ends of stripes are prone to dissolution. This explains the higher anodic disso-  
 217 lution rates and lower dissolution potentials of Pt(100) as compared to Pt(111),  
 218 where no similar destabilised atoms exist. After the potential exceeds that for 1  
 219 ML  $\text{O}_{\text{ads}}$  coverage (1.09 V), the dissolution can also take place during the first  
 220 extraction step.

221 The initial reversibility of PE and stability against cathodic dissolution on  
 222 Pt(111) can be attributed to the on-top arrangement found in our SXRD and

223 DFT studies, when the  $\text{Pt}_{ex}$  coverage is low and the Pt(111) lattice around the  
 224 vacancy on which the  $\text{O}_{ads}$  atoms are adsorbed remains intact. This on-top  
 225 geometry facilitates back insertion of the  $\text{Pt}_{ex}$  into the vacancy after desorption  
 226 of oxygen in the reduction process ( $\Delta G_{ex} = -0.5$  eV at  $\theta_O = 0.44$  ML, Extended  
 227 Data Fig. 4) rather than formation of a Pt adatom - vacancy pair via detach-  
 228 ment or dissolution in the form of  $\text{Pt}^{2+}$  as discussed in Ref. 15. At higher  $\text{Pt}_{ex}$   
 229 coverage the oxide surface structure is more complex, impeding straightforward  
 230 conclusions on the exact restructuring process. However, the increasing devi-  
 231 ations of the  $\text{Pt}_{ex}$  from the on-top positions, observed by SXRD,<sup>18</sup> suggest a  
 232 gradual loss of the overall integrity of the Pt surface lattice, which may account  
 233 for the irreversible surface roughening during subsequent oxide reduction as well  
 234 as for Pt cathodic dissolution.  
 235 In contrast, on Pt(100) we expect Pt adatoms and  $\text{Pt}^{2+}$  formation directly from  
 236 the ends of the  $\text{Pt}_{ex}$  stripes during oxide reduction. Similarly, adatoms and  $\text{Pt}^{2+}$   
 237 are also expected to form during the oxide reduction, i.e. upon a decrease in  
 238 the  $\text{O}_{ads}$  coverage. While the stripes are shortened, the remaining destabilised  
 239  $\text{Pt}_{ad}$  at the end of the stripe are more likely to dissolve or form adatoms.

## 240 Conclusion

241 In conclusion, the onset potentials of anodic dissolution on Pt(100) and Pt(111)  
 242 correspond to the onset of irreversibility in the extraction of the first Pt atoms  
 243 from their lattice sites as the surface is oxidized. According to our combined  
 244 SXRD and DFT studies, the marked difference in behaviour of the two surfaces  
 245 has its origin in the different atomic structures of the initial oxide. On Pt(111),  
 246 the extracted Pt atom lies directly above its original site, and reversibility for  
 247 low coverages is explained by its facile return to that site. However, on Pt(100)  
 248 the extracted Pt atom moves laterally away from its original site and initiates  
 249 immediate extraction of a second atom, leading to the formation of a stripe  
 250 structure. This mechanism produces unstable surface atoms at the stripe ends,  
 251 which can be dissolved both during the oxidation itself and during subsequent  
 252 oxide reduction, making the process irreversible from its onset.

253 As shown by our data, the precise Pt extraction mechanisms during oxida-  
 254 tion and the accompanying dissolution differ substantially on different Pt facets.  
 255 This sensitivity of Pt electrocatalyst degradation on surface structure has to be  
 256 taken into account in the quest for a knowledge-based approach, where highly  
 257 stable catalysts are ideally predicted *ab initio*. While our study represents the  
 258 first step in developing an atomistic picture of these processes for surfaces other  
 259 than Pt(111) (which may be considered as an atypical case according to the  
 260 results presented here), further studies are necessary, especially of more open  
 261 high-index surfaces. Such detailed insight into the degradation mechanisms of  
 262 structurally defined model systems is an important prerequisite for the chal-  
 263 lenging task of *ab initio* modelling the stability of real catalyst particles and,  
 264 ultimately, developing rational strategies for the design of catalysts with im-  
 265 proved stability.

## 266 Methods

### 267 Sample preparation.

268 All experiments employed cylindrical Pt single crystals (Mateck, Crystal Prepa-  
269 ration Laboratory) and Ar-purged 0.1 M HClO<sub>4</sub> solution made from ultrapure  
270 water and suprapur<sup>®</sup> perchloric acid (Merck). Potentials were measured versus  
271 Ag/AgCl (KCl<sub>sat.</sub>, SFC-ICP-MS or 3.4 M KCl, SXRD) reference electrodes but  
272 are reported against the reversible hydrogen electrode (RHE). The Pt crystals  
273 were initially cleaned in an ultra-high vacuum chamber using repeated Ar<sup>+</sup>-ion  
274 bombardment and subsequent annealing at 900 °C in 10<sup>-6</sup> mbar oxygen. Prior  
275 to each experiment, the Pt crystals were prepared by flame annealing with a  
276 butane torch (SFC-ICP-MS) or by annealing under 2 % CO/ 98 % Ar in an in-  
277 duction oven (Himmelwerk HU-2000+, SXRD). Subsequently, the sample was  
278 cooled in a flow of Ar/H<sub>2</sub> (SFC-ICP-MS) or 2 % CO/ 98 % Ar (SXRD) and trans-  
279 ferred to the cell protected either by a drop of Ar saturated ultrapure water or  
280 the adsorbed CO layer (SXRD, only Pt(100)). Immersion into the electrolyte  
281 was performed under potential control at potentials in the double layer regime.  
282 After immersion, remaining adsorbed CO was removed by anodic stripping.

### 283 Dissolution measurements.

284 The dissolution measurements at low scan rate of 10 mV·s<sup>-1</sup> to resolve the onset  
285 potentials of dissolution were conducted using the classical scanning flow cell  
286 coupled to an inductively coupled plasma mass spectrometer technique (referred  
287 to as SFC-ICP-MS, NexION 300X, Perkin Elmer). The working electrode (WE)  
288 had a contact area of 0.035 cm<sup>2</sup>. The flow rate of the SFC-ICP-MS was ca.  
289 170 µL · min<sup>-1</sup>. <sup>187</sup>Re was used as an ICP-MS internal standard for platinum.  
290 A graphite rod was used as a counter electrode and a double junction Ag/AgCl  
291 (Metrohm) as a reference electrode. Details on the SFC-ICP-MS measurements  
292 are given in Ref. 34, 35. The CV experiments at relatively fast scan rates  
293 were carried out using a modification to the SFC-ICP-MS, referred to here  
294 as the CSFC-ICP-MS (capillary SFC-ICP-MS), which allows for significantly  
295 increased time-potential resolution.<sup>36</sup> By inserting a small capillary directly  
296 above the working electrode (Supplementary Figure 9) and connecting directly  
297 to the ICP-MS via self-aspiration (bypassing the use of the peristaltic pump)  
298 delay times between the dissolution on the WE and ICP-MS detection can be  
299 reduced from ca. 25 to 3 s. Reduced delay times and shorter tubing distances  
300 limit the dispersion of dissolved species, and therefore enhance the resolution of  
301 dissolution rate profiles, e.g. to clearly separate anodic and cathodic dissolution  
302 signals.<sup>37</sup> The relatively fast flow rate of 580 µL · min<sup>-1</sup> resulted in a collection  
303 efficiency >99 %. Further details on this new technique can be found in Ref.  
304 38.

## 305 Electrochemical cell for surface x-ray diffraction.

306 All Surface X-ray Diffraction (SXRD) experiments employed the established  
307 SXRD electrochemical cell, described in Ref. 39. Inside this cell, the upward  
308 facing single-crystalline surface of the crystal sample is in contact with the elec-  
309 trolyte via a free-standing meniscus. This geometry is similar to the hanging  
310 meniscus geometry commonly used in single crystal electrochemistry and min-  
311 imises contributions from the defect-rich edges of the crystal. The amount of  
312 electrolyte inside the cell was controlled remotely using a motorised pump sys-  
313 tem with a precision of 1  $\mu\text{l}$ . To prevent oxygen contamination, the meniscus was  
314 kept in Ar atmosphere and the electrolyte reservoirs were continuously purged  
315 with Ar. We used a high-purity Pt foil with a surface area of about  $120\text{ mm}^2$  as  
316 counter electrode and a Ag/AgCl (3.4 M KCl, eDAQ) reference electrode. The  
317 reference electrode was connected by a micron-sized hole to a glass capillary,  
318 which was filled with 0.1 M  $\text{HClO}_4$  and served as Luggin capillary and salt  
319 bridge. This arrangement effectively ensured negligible leakage of KCl from the  
320 reference electrode to the cell. The cell and all glassware and tubing that were  
321 in contact with the electrolyte had been previously cleaned by soaking in a 4:1  
322 mixture of concentrated  $\text{H}_2\text{SO}_4$  and 30 %  $\text{H}_2\text{O}_2$  for at least 1 day. Afterwards,  
323 all materials were rinsed and boiled repeatedly in high-purity water (Elga pure-  
324 lab ultra  $18.2\text{ M}\Omega\text{ cm}$ ). Cyclic voltammograms (CVs) of Pt(111) and Pt(100)  
325 in 0.1 M  $\text{HClO}_4$  in the double layer potential region, prepared in this way and  
326 measured in the SXRD electrochemical cell, are shown in Extended Data Fig-  
327 ure 1. For both surfaces, the voltammograms are in good agreement with those  
328 reported in the literature.<sup>29</sup> CVs up to 0.6 V were recorded at the beginning of  
329 every SXRD experiment to check that a high surface quality had been obtained  
330 by the annealing process.

## 331 Surface x-ray diffraction setup.

332 All SXRD experiments were performed at undulator beamlines ID03 and ID31  
333 of the European Synchrotron Radiation Facility using a six-circle geometry and  
334 constant incident angle. A schematic illustration of the experimental setup is  
335 shown in Supplementary Figure 6. The crystal inside the SXRD cell was po-  
336 sitioned with the surface facing upwards. Conventional SXRD studies were  
337 performed at beamline ID03 and focused on kinetic studies of the Pt oxidation  
338 process by measuring the X-ray intensity at a fixed position along a crystal  
339 truncation rod (CTR). Similar as in our previous studies,<sup>17, 18, 23, 24, 40</sup> these  
340 measurements employed a photon energy of 22.5 keV, a (vert./hor.) beam size  
341 of  $45 \times 750\text{ }\mu\text{m}^2$  and an angle of incidence of  $0.3^\circ$ . A small 2D detector (Max-  
342 ipix) mounted on the diffractometer arm was used to simultaneously measure  
343 the crystal truncation rod (CTR) intensity and the background intensity with a  
344 time resolution of 0.1 s. The structure factor of the CTR at the studied reciproc-  
345 al space position was determined by first subtracting the background intensity  
346 and then taking the square root of the integrated diffraction rod intensity.  
347 *Operando* high-energy SXRD (HESXRD) measurements of the Pt(100) CTRs

348 were performed at the high-energy beamline ID31 at a photon energy of 68  
 349 keV. To enhance the surface contribution, the incident angle was kept at  $0.05^\circ$ ,  
 350 which is below the critical angle of total external reflection. The beam size  
 351 at the sample position was  $12 \times 48 \mu\text{m}^2$ . The orientation of the surface normal  
 352 direction was aligned better than  $0.005^\circ$  relative to the in-plane rotation axis,  
 353 to ensure that the angle of incidence did not change during sample rotation.  
 354 The diffracted X-ray intensity was recorded with a stationary, large-area X-ray  
 355 detector (Pilatus 2M CdTe), which was positioned 73 cm behind the sample.  
 356 This allowed covering a range of up to  $12 \text{ \AA}^{-1}$  momentum transfer perpendicular  
 357 to the surface and a range of about  $\pm 5.5 \text{ \AA}^{-1}$  momentum transfer parallel to  
 358 the surface. The tilt angles between the detector plane and the incident beam  
 359 direction were determined by recording the Debye-Scherrer rings of a  $\text{CeO}_2$  powder  
 360 calibration standard and analysing these data with the *pyFAI* software.<sup>41</sup>  
 361 The calculations of the reciprocal space coordinates for each detector pixel were  
 362 performed using the tilt-corrected angles. The position of all visible Bragg re-  
 363 flections on the detector and the corresponding observed sample rotations were  
 364 used to accurately determine the orientation of the crystal as described in Ref.  
 365 42. After mounting and alignment of the Pt sample, the positions of the  $\approx$   
 366 30 Bragg reflections from the bulk crystal were masked using small W pieces,  
 367 placed directly in front of the 2D detector. This is necessary to prevent damage  
 368 to the detector by the intense Bragg reflections, while measuring the weak CTR  
 369 intensities with the unattenuated incident beam. The beamstops manifest as  
 370 black areas on the detector frames (see Supplementary Figure 8 and missing  
 371 data points in the CTR profiles). In addition, the incident beam was blocked  
 372 by a beamstop located about 10 cm behind the sample, to reduce air scattering  
 373 background.  
 374 Points in reciprocal space were described in terms of the Miller indices  $(H K L)$ ,  
 375 where  $H$  and  $K$  correspond to reciprocal lattice unit cell vectors  $\vec{b}_1$  and  $\vec{b}_2$   
 376 in the surface plane and  $L$  to a vector  $\vec{b}_3$  along the surface normal. For  
 377 Pt(100) we chose the conventional cubic reciprocal basis with lattice vectors  
 378  $|\vec{b}_1| = |\vec{b}_2| = |\vec{b}_3| = 2\pi/a$  with  $a = 3.9242 \text{ \AA}$  being the Pt lattice constant. In  
 379 the case of Pt(111) we used a hexagonal unit cell with reciprocal lattice vectors  
 380 of length  $|\vec{b}_1| = |\vec{b}_2| = 8\pi/\sqrt{6}a$  and  $|\vec{b}_3| = 2\pi/\sqrt{3}a$ , which is common in SXRD  
 381 studies of fcc(111) surfaces.<sup>43</sup> A schematic illustration of the reciprocal space  
 382 geometry of Pt(111) and Pt(100) is shown in Supplementary Figure 7. The  
 383 Bragg reflections of Pt(111) are separated by  $\Delta L_{\text{Bragg}} = 3$  and the ones for  
 384 Pt(001) are separated by  $\Delta L_{\text{Bragg}} = 2$  along the CTRs. The absence of some  
 385 CTRs, such as  $(1 0 L)$ ,  $(2 1 L)$ , etc. for Pt(100), is related to the chosen fcc  
 386 unit cell.

### 387 Determination of the CTR structure factors.

388 Crystal truncation rod (CTR) data are commonly presented by plotting the  
 389 structure factor  $F_{HKL}$  as a function of  $L$ . To determine these structure factors  
 390 by HESXRD, the reciprocal space is mapped by continuously recording detector

frames during a single rotation of the crystal around the surface normal.<sup>30</sup> By summing up all the detector frames recorded during a reciprocal space mapping, the CTRs can be directly visualized (Supplementary Figure 8, vertical lines). Since the unit cell of Pt(100) has a rotational symmetry of  $90^\circ$ , a  $110^\circ$  rotation was sufficient to collect all symmetrically non-equivalent CTRs. An angular resolution of  $0.05^\circ$  was chosen to achieve high enough reciprocal space resolution at the low  $L$  values of the  $(3\ 1\ L)$  CTR. From these data, the CTR structure factors were determined using the *binoculars* software.<sup>44</sup> Here, first correction factors for solid angle and polarisation are applied to the measured intensities.<sup>45</sup> Then, a 3D representation of the reciprocal space is calculated by binning the intensities of each individual pixel, using the reciprocal space coordinates on each frame. For the analysis of the Pt(100) data, bin sizes of  $\Delta H = 0.002$ ,  $\Delta K = 0.002$  and  $\Delta L = 0.03$  were used. This corresponds to a series of  $HK$ -slices along the CTR, which are separated by the distance  $\Delta L$ . Within this  $\Delta L$  range, the structure factor  $F_{HKL}$  of the CTR is assumed to be constant and was determined by taking the square root of the integrated X-ray intensity at the CTR position. The background intensity was integrated in a region close to the CTR position and was subtracted from the CTR intensity. A more detailed description of the direct structure factor extraction in reciprocal space is given in the paper by Drnec et al.<sup>46</sup> To obtain the statistical uncertainties  $\sigma_2$  of each reflection, we extended the *binoculars* software by a package that calculates these uncertainties according to Poisson statistics. The total number of measured reflections in each CTR dataset was between 1922 and 2005. After averaging of symmetry equivalent reflections, between 802 and 808 reflections were available for the structural analysis. The agreement factor  $\varepsilon$  of the symmetry equivalent reflections was  $0.08 \pm 0.07$ . The uncertainties of the averaged reflections were then calculated to  $\sigma = \sqrt{\varepsilon^2 F_{HKL}^2 + \sigma_2^2}$ .

## Fitting of structural models to the CTR data.

To obtain the atomic positions of the surface atoms, all CTRs of a given data set were jointly fitted by a surface structural model using a Python-based software, developed by us for the quantitative analysis of HESXRD data. In this software, the structure factors, calculated from the model using kinematic scattering theory,<sup>47</sup> are fitted to the experimentally observed structure factors by the least squares method. A detailed description of the analysis of the CTRs in the double layer region and in the region of oxide formation is given in Supplementary Note 2 and 3, respectively. The statistical errors of the best-fit parameters given in Supplementary Tables 1-4 were calculated with the covariance matrix method.<sup>48</sup> These errors only take into account the goodness of fit and the experimental errors of the observed reflections, which are given by the counting statistics and the agreement factor between symmetry equivalent reflections. Systematic errors due to the chosen fit model are not included here. Those can be estimated from Supplementary Table 4, where for two central parameters, the occupancy and height of the  $\text{Pt}_{ex}$  atoms, and three characteristic potentials, 1.07 V, 1.12 V and 1.17 V, the results of the best fits obtained by

435 four different surface models are given.

## 436 Computational methods.

437 The density functional theory calculations were carried out using the VASP  
438 code, version 5.3.5-avx.<sup>49</sup> The PAW method<sup>50</sup> was used to describe the inter-  
439 action between the core electrons and the valence electron density, described by  
440 means of a plane-wave basis set, and the PBE exchange-correlation functional.<sup>51</sup>  
441 In the optimization, we used a plane-wave cutoff of 450 eV, the convergence cri-  
442 terion for the atomic forces was  $0.05 \text{ eV} \cdot \text{\AA}^{-1}$  and dipole corrections were applied  
443 between periodically repeated images in the z-axis. In the 4-layer-thick ( $3 \times 3$ )  
444 Pt(111) and ( $3 \times 3$ ) Pt(100) slabs the two topmost layers and the adsorbates  
445 were fully relaxed, while the two bottommost layers were fixed. For both slabs  
446 the k-point sampling was ( $4 \times 4 \times 1$ ).  $\text{H}_2$  and  $\text{H}_2\text{O}$  were simulated in cubic boxes  
447 of  $3375 \text{\AA}^3$ , sampling the gamma point only. The free energies were approxi-  
448 mated as:  $G = E^{\text{DFT}} + \text{ZPE} - \text{TS} + G^{\text{solv}}$ . The zero-point-energy (ZPE) and  
449 vibrational-entropy ( $\text{TS}^{\text{vib}}$ ) corrections were calculated within the harmonic os-  
450 cillator approximation for the adsorbed species, whereas for  $\text{H}_2$  and  $\text{H}_2\text{O}$  the  
451 values were taken from thermodynamic tables (see Supplementary Tables 5 and  
452 6).<sup>52</sup> Solvation contributions to the adsorption energies ( $G^{\text{solv}}$ ) of  $\text{H}_2\text{O}_{\text{ads}}$  and  
453  $\text{OH}_{\text{ads}}$  were taken from previous studies.<sup>53,54</sup> Proton-electron transfers were  
454 modelled with the computational hydrogen electrode.<sup>55</sup> The Pourbaix dia-  
455 grams of Pt(111) and Pt(100) in Extended Data Fig. 5 were built following  
456 the methodology described in Ref. 56.

457 The energetics of Pt dissolution as  $\text{Pt}^{2+}$  and  $\text{PtOH}^+$  was evaluated based  
458 on the experimental standard dissolution potential of Pt of 1.18 V and that  
459 of the reaction, which is 1.20 V.<sup>52</sup> From those two reactions, we conclude that  
460  $\text{Pt}^{2+}$  is slightly favoured over  $\text{PtOH}^+$ , thermodynamically speaking. Besides,  
461 we note that the cohesive energy of bulk Pt provided by PBE is 5.54 eV, while  
462 in experiments it is 5.87 eV.<sup>57</sup> Thus, a correction of 0.33 eV needs to be applied.

463 In calculated Pourbaix diagrams (Extended Data Fig. 5), we observe that  
464  $\text{O}_{\text{ads}}$  (i) is more strongly adsorbed on Pt(111) compared to Pt(100) at the same  
465 coverage and (ii) adsorbs at twofold bridge sites on Pt(100) and at threefold fcc  
466 hollow sites on Pt(111) (Supplementary Table 5). At a given potential, the oxy-  
467 gen coverage ( $\theta_{\text{O}}$ ) is typically larger on Pt(100) with respect to Pt(111), due to  
468 lower lateral repulsion, and corresponding well with previous calculations.<sup>56,58</sup>

## 469 Acknowledgements

470 We acknowledge the European Synchrotron Radiation Facility for provision of  
471 SXRD facilities, and H. Isern and T. Dufrane for their help with the SXRD  
472 experiments. Funding is acknowledged from NSERC (grant RGPIN-2017-04045)  
473 and Deutsche Forschungsgemeinschaft (grants MA 1618/23 and CH 1763/5-1).



## 474 Author Contributions

475 All authors performed experimental work and were involved in the experiment  
476 design. T.F. and D.J.S.S. analysed SXRD and SFC-ICP-MS data respectively.  
477 F.C.-V. performed DFT calculations. T.F., J.D. and O.M.M. prepared the  
478 manuscript. All authors were involved in data interpretation and editing of the  
479 manuscript.

## 480 Competing Interests

481 The authors declare no competing interests.

## 482 Data availability

483 The raw X-ray data as well as the atomic coordinates of the optimized computa-  
484 tional models have been deposited in the repository <https://doi.org/10.5281/zenodo.3937672>.  
485 All other data supporting the findings of this study are available within the arti-  
486 cle and its Supplementary Information, or from the corresponding author upon  
487 reasonable request.

## 488 Code availability

489 The custom software for the analysis of the CTR data and the custom *binocu-*  
490 *lars* backend for HESXRD structure factor determination are deposited in the  
491 repository <https://doi.org/10.5281/zenodo.3941003>. All other software used for  
492 this study is publicly available or can be obtained from the corresponding author  
493 upon reasonable request.

## 494 References

- 495 [1] Meier, J. C. *et al.* Design criteria for stable Pt/C fuel cell catalysts. *Beil-*  
496 *stein J. Nanotech.* **5**, 44–67 (2014).
- 497 [2] Climent, V. & Feliu, J. M. Thirty years of platinum single crystal electro-  
498 chemistry. *J. Solid State Electrochem.* **15**, 1297–1315 (2011).
- 499 [3] Conway, B. E. & Jerkiewicz, G. Surface orientation dependence of oxide  
500 film growth at platinum single crystals. *J. Electroanal. Chem.* **339**, 123–146  
501 (1992).
- 502 [4] You, H., Zurawski, D. J., Nagy, Z. & Yonco, R. M. In-situ x-ray reflectivity  
503 study of incipient oxidation of Pt(111) surface in electrolyte solutions. *J.*  
504 *Chem. Phys.* **100**, 4699–4702 (1994).

- [5] Tidswell, I., Markovic, N. & Ross, P. Potential dependent surface structure of the Pt(1 1 1) electrolyte interface. *J. Electroanal. Chem.* **376**, 119 – 126 (1994).
- [6] Wakisaka, M., Udagawa, Y., Suzuki, H., Uchida, H. & Watanabe, M. Structural effects on the surface oxidation processes at pt single-crystal electrodes studied by x-ray photoelectron spectroscopy. *Energy Environ. Sci.* **4**, 1662 (2011).
- [7] Gómez-Marín, A. M. & Feliu, J. M. Oxide growth dynamics at Pt(111) in absence of specific adsorption: A mechanistic study. *Electrochim. Acta* **104**, 367–377 (2013).
- [8] Tanaka, H. *et al.* Infrared reflection absorption spectroscopy of OH adsorption on the low index planes of pt. *Electrocatalysis* **6**, 295–299 (2014).
- [9] Sugimura, F., Nakamura, M. & Hoshi, N. The oxygen reduction reaction on kinked stepped surfaces of pt. *Electrocatalysis* **8**, 46–50 (2016).
- [10] Huang, Y.-F., Kooyman, P. J. & Koper, M. T. M. Intermediate stages of electrochemical oxidation of single-crystalline platinum revealed by in situ Raman spectroscopy. *Nat. Commun.* **7**, 12440 (2016).
- [11] Sugimura, F. *et al.* In situ observation of Pt oxides on the low index planes of Pt using surface enhanced Raman spectroscopy. *Phys. Chem. Chem. Phys.* **19**, 27570–27579 (2017).
- [12] Furuya, N. & Shibata, M. Structural changes at various Pt single crystal surfaces with potential cycles in acidic and alkaline solutions. *J. Electroanal. Chem.* **467**, 85–91 (1999).
- [13] Itaya, K., Sugawara, S., Sashikata, K. & Furuya, N. In situ scanning tunneling microscopy of platinum (111) surface with the observation of monatomic steps. *J. Vac. Sci. Technol. A* **8**, 515–519 (1990).
- [14] Lopes, P. P. *et al.* Relationships between Atomic Level Surface Structure and Stability/Activity of Platinum Surface Atoms in Aqueous Environments. *ACS Catal.* **6**, 2536–2544 (2016).
- [15] Lopes, P. P. *et al.* Dynamics of electrochemical Pt dissolution at atomic and molecular levels. *J. Electroanal. Chem.* **819**, 123–129 (2018).
- [16] Sandbeck, D. J. *et al.* Dissolution of Platinum Single Crystals in Acidic Medium. *ChemPhysChem* **20**, 2997–3003 (2019).
- [17] Ruge, M. *et al.* Structural Reorganization of Pt(111) Electrodes by Electrochemical Oxidation and Reduction. *J. Am. Chem. Soc.* **139**, 4532–4539 (2017).

- [18] Ruge, M. *et al.* Electrochemical oxidation of smooth and nanoscale rough Pt(111): An in situ surface X-ray scattering study. *J. Electrochem. Soc* **164**, H608–H614 (2017).
- [19] Jacobse, L., Huang, Y.-F., Koper, M. T. M. & Rost, M. J. Correlation of surface site formation to nanoisland growth in the electrochemical roughening of Pt(111). *Nat. Mater.* **17**, 277–282 (2018).
- [20] Arulmozhi, N., Esau, D., Lamsal, R. P., Beauchemin, D. & Jerkiewicz, G. Structural transformation of monocrystalline platinum electrodes upon electro-oxidation and electro-dissolution. *ACS Catal.* **8**, 6426–6439 (2018).
- [21] Topalov, A. A. *et al.* Dissolution of Platinum: Limits for the Deployment of Electrochemical Energy Conversion? *Angew. Chem., Int. Ed.* **51**, 12613–12615 (2012).
- [22] Gómez-Marín, A. M. & Feliu, J. M. Pt(111) surface disorder kinetics in perchloric acid solutions and the influence of specific anion adsorption. *Electrochim. Acta* **82**, 558–569 (2012).
- [23] Drnec, J. *et al.* Initial stages of Pt(111) electrooxidation: dynamic and structural studies by surface X-ray diffraction. *Electrochim. Acta* **224**, 220 – 227 (2017).
- [24] Drnec, J., Harrington, D. & Magnussen, O. Electrooxidation of Pt(111) in acid solution. *Curr. Op. Electrochem.* **4**, 69–75 (2017).
- [25] Liu, Y., Barbour, A., Komanicky, V. & You, H. X-ray Crystal Truncation Rod Studies of Surface Oxidation and Reduction on Pt(111). *J. Phys. Chem. C* **120**, 16174–16178 (2016).
- [26] Fantauzzi, D., Mueller, J. E., Sabo, L., van Duin, A. C. T. & Jacob, T. Surface Buckling and Subsurface Oxygen: Atomistic Insights into the Surface Oxidation of Pt(111). *ChemPhysChem* **16**, 2797–2802 (2015).
- [27] Eslamibidgoli, M. J. & Eikerling, M. H. Atomistic Mechanism of Pt Extraction at Oxidized Surfaces: Insights from DFT. *Electrocatalysis* **7**, 345–354 (2016).
- [28] Gu, Z. & Balbuena, P. B. Chemical Environment Effects on the Atomic Oxygen Absorption into Pt(111) Subsurfaces. *J. Phys. Chem. C* **111**, 17388–17396 (2007).
- [29] Rodes, A., Zamakhchari, M. A., El Achi, K. & Clavilier, J. Electrochemical behaviour of Pt(100) in various acidic media: Part I. On a new voltammetric profile of Pt(100) in perchloric acid and effects of surface defects. *J. Electroanal. Chem.*, **305**, 115–129 (1991).
- [30] Gustafson, J. *et al.* High-Energy Surface X-ray Diffraction for Fast Surface Structure Determination. *Science* **343**, 758–761 (2014).

- [31] Devarajan, S. P., Hinojosa, J. A. & Weaver, J. F. STM study of high-coverage structures of atomic oxygen on Pt(1 1 1):  $p(2 \times 1)$  and Pt oxide chain structures. *Surf. Sci.* **602**, 3116–3124 (2008).
- [32] Van Spronsen, M. A., Frenken, J. W. & Groot, I. M. Observing the oxidation of platinum. *Nat. Commun.* **8** (2017).
- [33] Xing, L., Jerkiewicz, G. & Beauchemin, D. Ion exchange chromatography coupled to inductively coupled plasma mass spectrometry for the study of Pt electro-dissolution. *Anal. Chim. Acta* **785**, 16 – 21 (2013).
- [34] Cherevko, S., Kulyk, N. & Mayrhofer, K. J. Durability of platinum-based fuel cell electrocatalysts: Dissolution of bulk and nanoscale platinum. *Nano Energy* **29**, 275 – 298 (2016).
- [35] Cherevko, S., Topalov, A. A., Zeradjanin, A. R., Keeley, G. P. & Mayrhofer, K. J. J. Temperature-Dependent Dissolution of Polycrystalline Platinum in Sulfuric Acid Electrolyte. *Electrocatalysis* **5**, 235–240 (2014).
- [36] Geiger, S. *Stability investigations of iridium-based catalysts towards acidic water splitting*. doctoralthesis, Ruhr-Universität Bochum, Universitätsbibliothek (2018).
- [37] Lamsal, R. P., Jerkiewicz, G. & Beauchemin, D. Enhancement of the capabilities of inductively coupled plasma mass spectrometry using monosegmented flow analysis. *Anal. Chem.* **90**, 13842–13847 (2018).
- [38] Sandbeck, D. J. S. *On the Dissolution of Platinum: From Fundamental to Advanced Catalytic Materials*. doctoralthesis, Friedrich-Alexander-Universität Erlangen-Nürnberg (FAU) (2020).
- [39] Magnussen, O. M., Krug, K., Ayyad, A. H. & Stettner, J. In situ diffraction studies of electrode surface structure during gold electrodeposition. *Electrochim. Acta* **53**, 3449–3458 (2008).
- [40] Drnec, J. *et al.* Pt oxide and oxygen reduction at Pt(111) studied by surface X-ray diffraction. *Electrochem. Commun.* **84**, 50–52 (2017).
- [41] Ashiotis, G. *et al.* The fast azimuthal integration Python library: PyFAI. *J. Appl. Crystallogr.* **48**, 510–519 (2015).
- [42] Busing, W. R. & Levy, H. A. Angle calculations for 3- and 4-circle X-ray and neutron diffractometers. *Acta Crystallogr.* **22**, 457–464 (1967).
- [43] Wang, J., Ocko, B., Davenport, A. & Isaacs, H. In situ X-ray-diffraction and -reflectivity studies of the Au(111)/ electrolyte interface: reconstruction and anion adsorption. *Phys. Rev. B* **46**, 10321–10338 (1992).
- [44] Roobol, S., Onderwaater, W., Drnec, J., Felici, R. & Frenken, J. BINoculars: Data reduction and analysis software for two-dimensional detectors in surface X-ray diffraction. *J. Appl. Crystallogr.* **48**, 1324–1329 (2015).

- [45] Vlieg, E. Integrated Intensities Using a Six-Circle Surface X-ray Diffractometer. *J. Appl. Crystallogr.* **30**, 532–543 (1997).
- [46] Drnec, J. *et al.* Integration techniques for surface X-ray diffraction data obtained with a two-dimensional detector. *J. Appl. Crystallogr.* **47**, 365–377 (2014).
- [47] Feidenhans'l, R. Surface structure determination by X-ray diffraction. *Surf. Sci. Rep.* **10**, 105–188 (1989).
- [48] Press, W. H., Teukolsky, S. A., Vetterling, W. T. & Flannery, B. P. *Numerical Recipes in C: The Art of Scientific Computing. Second Edition* (Cambridge University Press, 1992).
- [49] Kresse, G. & Furthmüller, J. Efficient iterative schemes for ab initio total-energy calculations using a plane-wave basis set. *Phys. Rev. B* **54**, 11169–11186 (1996).
- [50] Kresse, G. & Joubert, D. From ultrasoft pseudopotentials to the projector augmented-wave method. *Phys. Rev. B* **59**, 1758–1775 (1999).
- [51] Perdew, J. P., Burke, K. & Ernzerhof, M. Generalized Gradient Approximation Made Simple. *Phys. Rev. Lett.* **77**, 3865–3868 (1996).
- [52] Lide, D. R. (ed.) *CRC Handbook of Chemistry and Physics, 85th Edition* (CRC Press, 2005).
- [53] Calle-Vallejo, F., de Morais, R., Illas, F., Loffreda, D. & Sautet, P. Affordable Estimation of Solvation Contributions to the Adsorption Energies of Oxygenates on Metal Nanoparticles. *J. Phys. Chem. C* **123**, 5578–5582 (2019).
- [54] He, Z.-D., Hanselman, S., Chen, Y.-X., Koper, M. T. M. & Calle-Vallejo, F. Importance of Solvation for the Accurate Prediction of Oxygen Reduction Activities of Pt-Based Electrocatalysts. *J. Phys. Chem. Lett.* **8**, 2243–2246 (2017).
- [55] Nørskov, J. K. *et al.* Origin of the Overpotential for Oxygen Reduction at a Fuel-Cell Cathode. *J. Phys. Chem. B* **108**, 17886–17892 (2004).
- [56] Hansen, H. A., Rossmeisl, J. & Nørskov, J. K. Surface Pourbaix diagrams and oxygen reduction activity of Pt, Ag and Ni(111) surfaces studied by DFT. *Phys. Chem. Chem. Phys.* **10**, 3722–3730 (2008).
- [57] Janthon, P. *et al.* Bulk Properties of Transition Metals: A Challenge for the Design of Universal Density Functionals. *J. Chem. Theory Comput.* **10**, 3832–3839 (2014).
- [58] Bizzotto, F. *et al.* Examining the Structure Sensitivity of the Oxygen Evolution Reaction on Pt Single-Crystal Electrodes: A Combined Experimental and Theoretical Study. *ChemPhysChem* **20** (2019).

# **Supplementary Information: Structure-dependence of the atomic-scale mechanisms of Pt electrooxidation and dissolution**

Timo Fuchs<sup>1</sup>, Jakub Drnec<sup>2</sup>, Federico Calle-Vallejo<sup>3</sup>, Natalie Stubb<sup>4</sup>, Daniel J. S. Sandbeck<sup>5,6</sup>,  
Martin Ruge<sup>1</sup>, Serhiy Cherevko<sup>5</sup>, David A. Harrington<sup>4</sup> & Olaf M. Magnussen<sup>1\*</sup>

<sup>1</sup>*Institut für Experimentelle und Angewandte Physik, Christian-Albrechts-Universität zu Kiel, Olshausenstr. 40, 24098 Kiel, Germany*

<sup>2</sup>*Experimental division, European Synchrotron Radiation Facility, 71 Avenue des Martyrs, 38000 Grenoble, France*

<sup>3</sup>*Departament de Ciència de Materials i Química Física & Institut de Química Teòrica i Computacional (IQTUB), Universitat de Barcelona, Martí i Franquès 1, 08028 Barcelona, Spain.*

<sup>4</sup>*Chemistry Department, University of Victoria, Victoria, British Columbia, V8W 2Y2, Canada*

<sup>5</sup>*Helmholtz-Institute Erlangen-Nürnberg for Renewable Energy (IEK-11), Forschungszentrum Jülich GmbH, 91058 Erlangen, Germany*

<sup>6</sup>*Department of Chemical and Biological Engineering, Friedrich-Alexander-Universität Erlangen-Nürnberg, 91058 Erlangen, Germany*

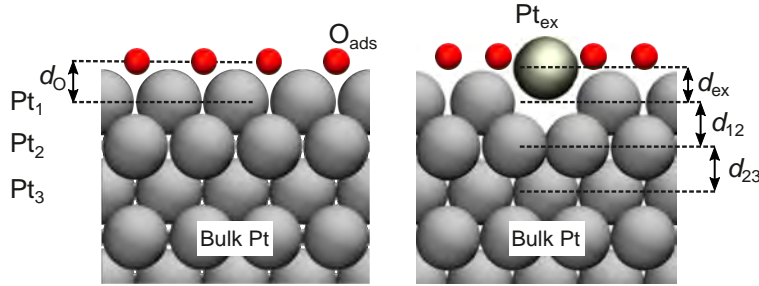
\* Corresponding author

## Supplementary Note 1: Overview of CTR measurements

CTR data sets of Pt(100) were obtained at two potentials in the double layer region, 0.12 and 0.95 V, and at the following 6 potentials in the Pt oxidation region: 0.984, 1.00, 1.02, 1.07, 1.12 and 1.17 V. At each potential 11 CTRs were measured up to  $L$  values of 7.5, of which the following are symmetrically equivalent:

- $(1\ 1\ L)$ ,  $(-1\ -1\ L)$
- $(0\ 2\ L)$ ,  $(0\ -2\ L)$ ,  $(2\ 0\ L)$
- $(2\ 2\ L)$ ,  $(-2\ -2\ L)$
- $(1\ 3\ L)$ ,  $(-1\ -3\ L)$ ,  $(3\ 1\ L)$ ,  $(1\ -3\ L)$

The full data for 4 different potentials are displayed in Extended Data Fig. 3. Coloured lines show the results of best fits by the models presented in Supplementary Figure 1, which are discussed in the following sections. The CTR data obtained at other potentials are in full accordance with the presented results.

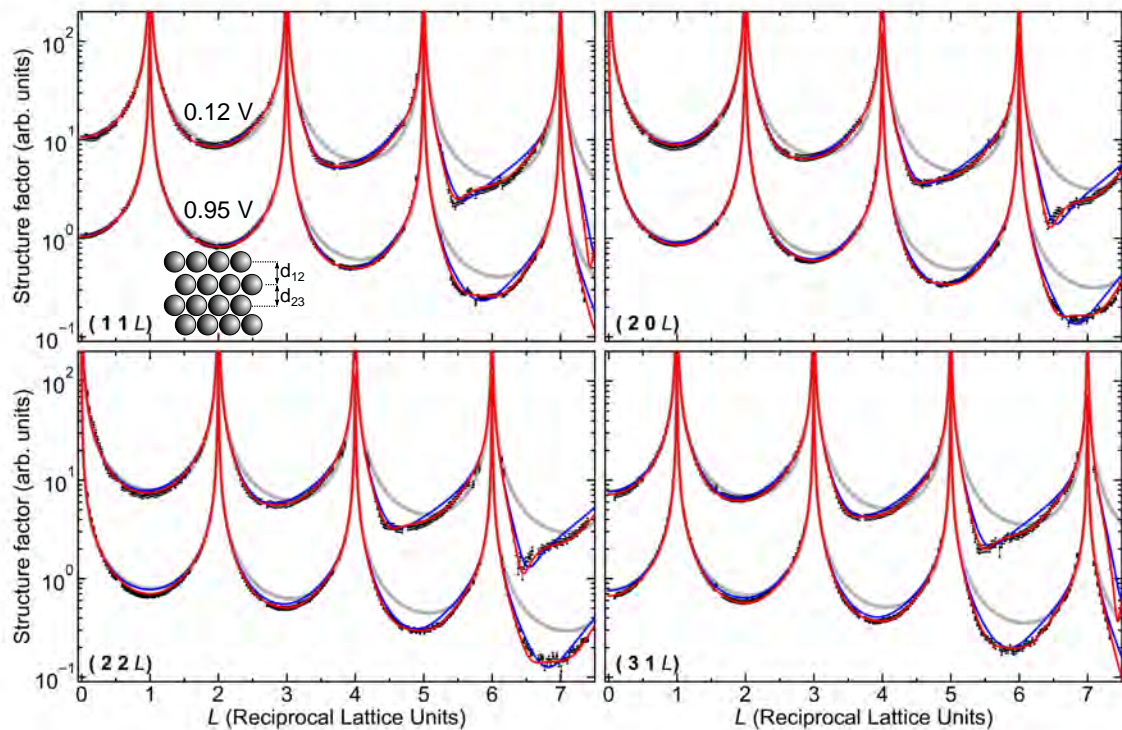


**Supplementary Figure 1.** Schematic illustration of the models used for fitting of the CTR data of Pt(100) at (a): 0.95 V and (b): 1.07, 1.12 and 1.17 V. Free fit parameters were the interplanar distances  $d_{ex}$ ,  $d_{12}$  and  $d_{23}$ , the coverage of the exchanged Pt<sub>ex</sub> atoms  $\theta_{ex}$  and the mean displacements  $\Delta r_i$  of the respective position of the atoms Pt<sub>*i*</sub>, corresponding to the Debye-Waller factors. The in-plane component  $(\Delta r_i)_{\parallel}$  and out-of-plane component  $(\Delta r_i)_{\perp}$  of the mean atomic displacements have been fitted individually.

## Supplementary Note 2: Initial surface quality and structure in the double layer region

The initial surface quality of the freshly prepared Pt(100) surface was characterised in the region of H adsorption and OH adsorption (0.12 V and 0.95 V). At those potentials only the CTRs were observed; additional in-plane peaks associated with a reconstructed surface were not found. The measured, as well as the calculated CTRs of a bulk-terminated crystal are shown in Supplementary Figure 2. At small  $L$ , the measured structure factor is close to the rod profile of a bulk-terminated crystal, indicating a surface with a very small defect density. However, with increasing  $L$  the curves gradually deviate from the rods of the bulk-terminated crystal. This can be attributed to higher vertical Debye-Waller factor of the surface atoms compared to the bulk Debye-Waller factor. A shift of the minima to lower  $L$  can be assigned to a lattice expansion of the top Pt layers. Overall, these effects are more pronounced in the region of H adsorption, which is in good agreement with Tidswell et al. who found a larger lattice expansion of the very first Pt layer in the region of H adsorption than in the region of OH adsorption.<sup>1</sup> For further quantitative analysis we used a model of an unreconstructed surface with either one or two expanded top Pt layers. Adsorbed hydrogen was not included in the model since the X-ray scattering from hydrogen is negligible at high energies. Water layering was also not included, because it does not contribute to the non-specular CTRs given its low in-plane order. Free fit parameters were  $d_{12}$  and  $d_{23}$  and the in-plane and out-of-plane Debye-Waller factors of the Pt<sub>1</sub> and Pt<sub>2</sub> layer. The bulk Debye-Waller factor has been fitted freely at the diffraction rod at 0.12 V. The corresponding fits using the two models, one layer and two layers relaxation, are shown in Supplementary Figure 2 and the best-fit parameters are given in Supplementary Table 1.





**Supplementary Figure 2.** CTRs of Pt(001) at 0.12 V in the region of  $H_{ads}$  and at 0.95 V in the region of  $OH_{ads}$  close to the onset of oxidation. The grey lines are the CTRs of a bulk terminated surface. Blue and red lines show CTR fits with vertical relaxations ( $d_{12}$ ,  $d_{23}$ ) of one or two Pt layers, respectively.

$E_{RHE}$	0.95 V		0.12 V	
Model	2 relaxed layers	1 relaxed layer	2 relaxed layers	1 relaxed layer
$d_{12}/\text{\AA}$	$1.9892 \pm 0.0005$	$1.9893 \pm 0.0005$	$2.0147 \pm 0.0006$	$2.0175 \pm 0.0005$
$d_{23}/\text{\AA}$	$1.96948 \pm 0.00024$		$1.97191 \pm 0.00028$	
$(\Delta r_1)_{\parallel}/\text{\AA}$	$0.1034 \pm 0.0021$	$0.077 \pm 0.004$	$0.0946 \pm 0.0026$	$0.074 \pm 0.004$
$(\Delta r_2)_{\parallel}/\text{\AA}$	$0.0742 \pm 0.0019$		$0.0785 \pm 0.0022$	
$(\Delta r_1)_{\perp}/\text{\AA}$	$0.1096 \pm 0.0004$	$0.1054 \pm 0.0005$	$0.1030 \pm 0.0004$	$0.0972 \pm 0.0007$
$(\Delta r_2)_{\perp}/\text{\AA}$	$0.0844 \pm 0.0004$		$0.0847 \pm 0.0005$	
$\chi_r^2$	1.05	3.04	0.67	1.81

**Supplementary Table 1.** Structure parameters of the pristine surface at 0.12 V and 0.95 V obtained by fitting of the diffraction rods. Two models have been considered either with one expanded Pt layer or two expanded Pt layers. Errors are estimated from the diagonals of the covariance matrix.

As expected, the data at 0.12 V and 0.95 V can be described well with an unreconstructed surface. The fit with an increased interplanar distance  $d_{12}$  is already in good agreement with the data, but inclusion of a second expanded interplanar distance  $d_{23}$  does significantly improve the fit. Note that the differences in both models are only becoming apparent at very high  $L$ , which is not commonly measured in conventional SXRD, since it requires very long data acquisition times and is above the range of movement for most diffractometers.

After inclusion of 2 relaxed Pt layers, the fit matches the data within the experimental errors, with  $\chi_r^2 = 1.05$  and  $\chi_r^2 = 0.67$  for the data sets at 0.95 V and 0.12 V, respectively. Allowing additionally for surface roughness by reducing the coverage of the topmost Pt layer does not improve the fit in either of the models, indicating that the initial Pt surface is atomically smooth. The fit of the data set at 0.12 V yields an expansion of 2.68 % relative to the interplanar distance of the Pt bulk lattice ( $d = 1.9621 \text{ \AA}$ ). This is higher than the value obtained in a similar experiment by Tidswell et al., who found an expansion of up to 1 %. However, the amount of surface defects was much higher than in our case, which may explain the difference. The best fit shown in Extended Data Fig. 2 is the CTR fit with 2 relaxed Pt layers.

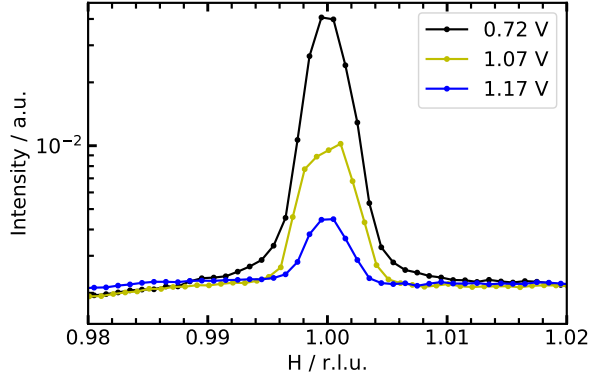
The adsorption of oxygen species at 0.95 V is indicated by a reduction of the Pt layer expansion to 1.38 %. However, inclusion of adsorbed oxygen species in the surface model has only a minor effect on the fit quality, independent of the chosen  $O_{ads}$  adsorption site (top, bridge, hollow), because its scattering contribution can be easily compensated by small changes in the Pt distances and Debye-Waller factors. Nevertheless, it is clear that oxygen is present on the surface at this potential. We therefore included an adsorbed oxygen monolayer in the fit of the data at 0.95 V

presented in Fig. 2, with the oxygen site and coverage being chosen according to the results of the DFT calculations. This results in  $\chi_r^2 = 1.01$ , i.e., a marginally better value as compared to the model without  $O_{ads}$ .

The Debye-Waller factor for the bulk Pt atoms, obtained in this final fit of the data at 0.12 V ( $\Delta r_{bulk} = 0.0743 \text{ \AA}$ ), was used as a fixed parameter in the subsequent analysis of the surface oxide.

### **Supplementary Note 3: CTR analysis of the Pt(100) oxide**

The oxide studied in the CTR analysis was formed by linearly sweeping the potential by 50 mV/s to a given potential in the region of oxide formation, and subsequently holding the potential at this value for 5 min before starting data acquisition. This ensures that the oxide structure has reached a quasi-stationary state, in which residual slow changes in the oxide structure<sup>2</sup> are negligible over the time of the measurement. During the HESXRD measurement, the potential was kept constant. After the first measurement at 0.12 V, the potential was increased by a linear sweep and the measurement was repeated at the next potential after 5 min of holding time. This procedure was carried out for potentials 0.95 V, 0.98 V, 1.00 V, 1.02 V, 1.07 V, 1.12 V and 1.17 V. At none of these potentials additional diffraction peaks or rods associated with a well-ordered oxide were observed. Furthermore, no increase in background scattering due to diffuse scattering from the oxide can be observed, suggesting that this signal is too weak to be distinguishable from the liquid background scattering. The latter is illustrated in Supplementary Figure 3, where the intensity distribution along the H-direction at the (1 1 2) position is shown as an example.



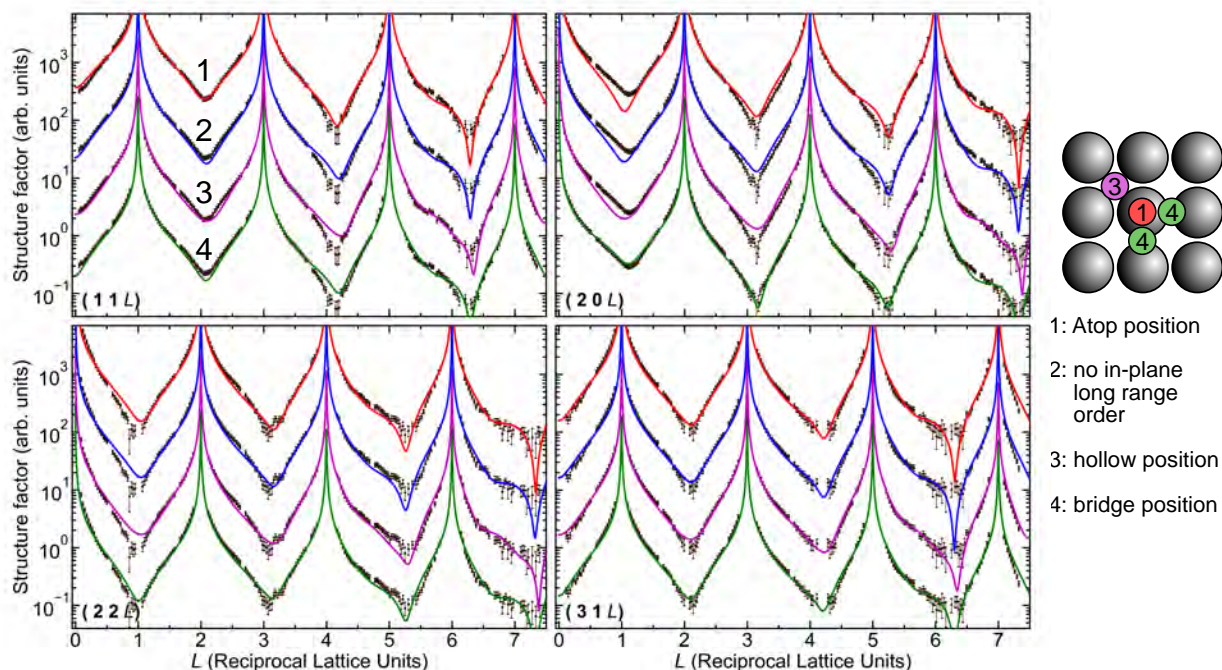
**Supplementary Figure 3.** Scattering along the H-direction at the (1 1 2) position of Pt(100) at different potentials in the oxidation region (1.07 V, 1.17 V) and prior oxidation at 0.72 V. No increase of background scattering adjacent to the CTR is observed. Note that these measurements were performed at a lower photon energy of 22.5 keV at ID03 to increase the reciprocal space resolution.

$E_{\text{RHE}}$	1.17 V	1.12 V	1.07 V	0.95 V
$\theta_{\text{ex}}/\text{ML}$	$0.583 \pm 0.006$	$0.405 \pm 0.007$	$0.213 \pm 0.008$	
$d_{\text{ex}}/\text{\AA}$	$1.407 \pm 0.011$	$1.409 \pm 0.014$	$1.29 \pm 0.04$	
$d_{\text{O}}/\text{\AA}$	$2.069 \pm 0.020$	$2.15 \pm 0.04$	$1.97 \pm 0.08$	$1.797 \pm 0.026$
$d_{12}/\text{\AA}$	$1.9271 \pm 0.0011$	$1.9436 \pm 0.0011$	$1.9592 \pm 0.0009$	$1.9889 \pm 0.0005$
$d_{23}/\text{\AA}$	$1.9794 \pm 0.0005$	$1.9702 \pm 0.0006$	$1.9692 \pm 0.0005$	$1.96944 \pm 0.00024$
$(\Delta r_{\text{ex}})_{\parallel}/\text{\AA}$	$0.493 \pm 0.008$	$0.541 \pm 0.018$	$0.35 \pm 0.04$	
$(\Delta r_{\text{O}})_{\parallel}/\text{\AA}$	$0.30 \pm 0.04$	$0.40 \pm 0.06$	$0.21 \pm 0.05$	$0.44 \pm 0.04$
$(\Delta r_1)_{\parallel}/\text{\AA}$	$0.074 \pm 0.014$	$0.091 \pm 0.009$	$0.102 \pm 0.006$	$0.1047 \pm 0.0021$
$(\Delta r_2)_{\parallel}/\text{\AA}$	$0.079 \pm 0.005$	$0.085 \pm 0.004$	$0.074 \pm 0.004$	$0.0742 \pm 0.0019$
$(\Delta r_{\text{ex}})_{\perp}/\text{\AA}$	$0.202 \pm 0.011$	$0.175 \pm 0.021$	$0.258 \pm 0.027$	
$(\Delta r_{\text{O}})_{\perp}/\text{\AA}$	$0.07 \pm 0.05$	$0.07 \pm 0.07$	$0.173 \pm 0.027$	$0.08 \pm 0.04$
$(\Delta r_1)_{\perp}/\text{\AA}$	$0.0858 \pm 0.0026$	$0.0967 \pm 0.0019$	$0.1112 \pm 0.0009$	$0.1089 \pm 0.0004$
$(\Delta r_2)_{\perp}/\text{\AA}$	$0.1011 \pm 0.0010$	$0.0962 \pm 0.0009$	$0.0922 \pm 0.0007$	$0.0843 \pm 0.0004$
$\chi_r^2$	3.182	3.21	1.977	1.013

**Supplementary Table 2.** Structural parameters of the potential dependent oxide structure of Pt(100) in steady-state obtained from a fit of the CTRs in Fig. 2 and Extended Data Fig. 3. Errors are estimated from the diagonals of the covariance matrix.

The CTRs obtained at 0.95, 1.07, 1.12 and 1.17 V are displayed in Fig. 2 and Extended Data Fig. 3. The CTRs at 0.98 V, 1.00 V and 1.02 V are not shown here, because there are only a very minor changes in the profiles up to 1.02 V. At 1.07 V, the structure factor at all anti-Bragg positions starts to drop below that of a bulk-terminated crystal, indicating an increased roughness of the surface. Interestingly, the minimum at (2 2 1) drops slightly lower than the minimum at

(2 2 3), while (2 2 5) is again lower than what would be expected from the increased Debye-Waller factor alone. A similar behaviour can be seen at (2 0 1), (2 0 3) and (2 0 5), but here the relationship between the relative heights of the minima is inverted. This feature can be explained by a modulation of the CTRs by an oscillation with a periodicity of about  $\Delta L \approx 4$ . One possible cause for that is a change in the interplanar distance of about half of the bulk lattice spacing. To exemplifying the differences in the CTRs caused by different surface oxide structures, we discuss fits of the CTR data at 1.12 V by selected models. As already discussed in the previous section, variation of the interplanar distances of the two top Pt layers is necessary to adequately describe an undisturbed Pt(100) surface in the double layer region. After oxidation, the increased roughness can be described by at least one additional partially occupied Pt layer at the surface, representing the Pt atoms in the newly formed oxide. The dissolution of Pt in the initial stages of oxidation is below 1  $\mu\text{ML}$ , as can be calculated from Fig. 1 with conversion factors of  $1.30 \cdot 10^{15}$  and  $1.49 \cdot 10^{15}$  atoms/ $\text{cm}^2$  for surface atomic densities of Pt(100) and Pt(111), respectively. This very small loss in the number of Pt surface atoms is far below the detection limit of SXRD. We therefore assume in our models that the overall number of Pt atoms on the surface is conserved and that all extracted Pt atoms are bound in the formed Pt surface oxide. In total, four possible lateral locations of the  $\text{Pt}_{ex}$  atoms were considered in the modelling, which are illustrated in Supplementary Figure 4. In the models, the  $\text{Pt}_{ex}$  were placed either in atop (1), hollow (3) or bridge (4) sites. Furthermore, an oxide structure was considered where the  $\text{Pt}_{ex}$  form a layer without long-range order, i.e. are bound in an amorphous oxide (2). The vertical position of the extracted atoms was a free parameter of the fit. Best fits of the CTRs at 1.12 V using these models are shown in Supplementary Figure 4 and the



**Supplementary Figure 4.** CTR data of the oxide structure at 1.12 V and CTR fits with different in-plane locations of the  $\text{Pt}_{ex}$  in the oxide structure. A graphic illustration at the top right corner shows the lateral position of the  $\text{Pt}_{ex}$  atom in the different oxide models. The fits and the diffraction rods in the graph are spaced vertically with an offset factor of 10.

corresponding fit parameters and reduced  $\chi_r^2$  are given in Supplementary Table 3. Models 1,2 and 3 show systematic deviations from the data, which are most prominent at (2 2 1), where the shift of the minimum towards lower  $L$  is only described well by the bridge site model (4). Similarly, the shift of the minimum of the CTR at (2 0 1) towards higher  $L$  is also only well represented by a fit using this oxide model. Also the lowest value of  $\chi_r^2$  is obtained using a fit of model 4. Furthermore, we assessed the influence of surface oxygen species on the CTR fits. A comparison of CTR fits with a model containing only the Pt atoms and with an additional monolayer of  $\text{O}_{ads}$  in bridge sites is shown in Supplementary Figure 5 for 0.95 V, 1.07 V, 1.12 V and 1.17 V. Similarly to the fit of the smooth surface at 0.95 V, inclusion of  $\text{O}_{ads}$  only leads to a small improvement of the fit, which is

<b>Pt<sub>ex</sub> location</b>	<b>atop (1)</b>	<b>disordered (2)</b>	<b>hollow (3)</b>	<b>bridge (4)</b>
$\theta_{ex}/\text{ML}$	$0.415 \pm 0.009$	$0.394 \pm 0.008$	$0.1948 \pm 0.0023$	$0.404 \pm 0.007$
$d_{ex}/\text{\AA}$	$2.22 \pm 0.04$		$1.9395 \pm 0.0030$	$1.409 \pm 0.016$
$d_{12}/\text{\AA}$	$1.9425 \pm 0.0013$	$1.9428 \pm 0.0013$	$1.9574 \pm 0.0012$	$1.9439 \pm 0.0011$
$d_{23}/\text{\AA}$	$1.9707 \pm 0.0008$	$1.9703 \pm 0.0007$	$1.9755 \pm 0.0007$	$1.9701 \pm 0.0006$
$(\Delta r_{ex})_{\parallel}/\text{\AA}$	$0.796 \pm 0.030$		$0.07 \pm 0.06$	$0.491 \pm 0.013$
$(\Delta r_1)_{\parallel}/\text{\AA}$	$0.087 \pm 0.011$	$0.097 \pm 0.009$	$0.075 \pm 0.014$	$0.093 \pm 0.008$
$(\Delta r_2)_{\parallel}/\text{\AA}$	$0.090 \pm 0.004$	$0.089 \pm 0.004$	$0.074 \pm 0.005$	$0.086 \pm 0.004$
$(\Delta r_{ex})_{\perp}/\text{\AA}$	$0.24 \pm 0.04$		$0.074 \pm 0.008$	$0.242 \pm 0.019$
$(\Delta r_1)_{\perp}/\text{\AA}$	$0.0965 \pm 0.0021$	$0.1011 \pm 0.0019$	$0.0953 \pm 0.0019$	$0.0973 \pm 0.0017$
$(\Delta r_2)_{\perp}/\text{\AA}$	$0.0947 \pm 0.0010$	$0.0954 \pm 0.0010$	$0.0937 \pm 0.0009$	$0.0955 \pm 0.0009$
$\chi_r^2$	4.285	4.443	3.51	3.229

**Supplementary Table 3.** Structural parameters of the 4 considered oxide structures obtained by fits of the CTRs at  $E = 1.12$  V, which are shown in Supplementary Figure 4. Errors are estimated from the diagonals of the covariance matrix.

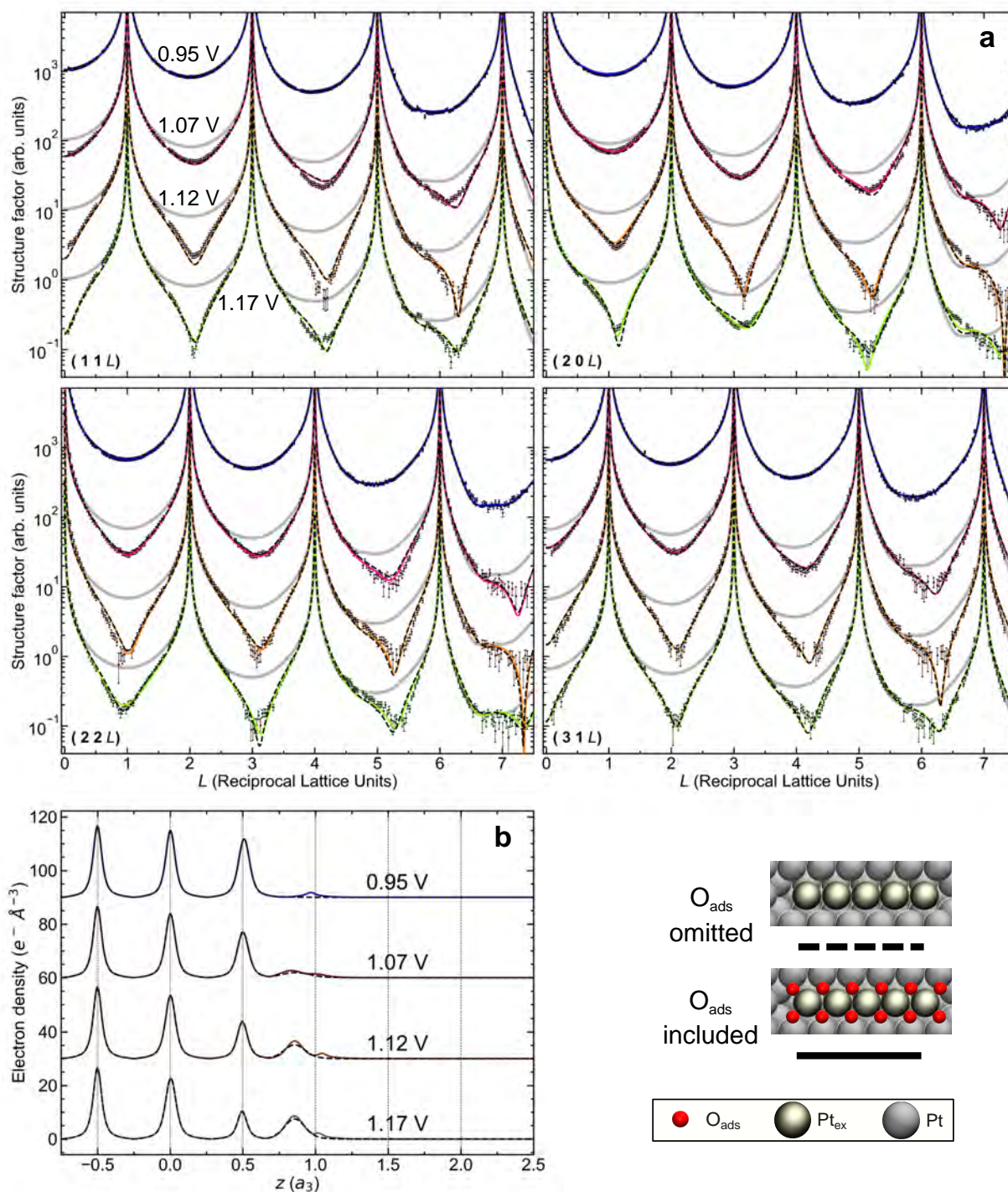
insufficient for an exact determination of the lateral  $O_{ads}$  locations. Nevertheless, a monolayer of  $O_{ads}$  was included in the model employed for the data in Fig. 2 as surface oxygen species obviously are present in the oxide. The lateral location of the  $O_{ads}$  was set to the bridge site configuration, predicted by the DFT calculations. Vertical spacing and coverage of the  $Pt_{ex}$  obtained from the fits with and without  $O_{ads}$  are given in Supplementary Table 4. In both cases, coverage and position of the  $Pt_{ex}$  are very similar. For the structural parameters of the Pt layers underneath the two models result in even smaller differences of 1-2%. In addition, we also performed fits (with and without  $O_{ads}$ ) in which also the third Pt layer was allowed to relax. These resulted in even lower  $\chi_r^2$  values, but the  $Pt_{ex}$  vertical position and coverage remained very similar.

The above results demonstrate clearly that the location of the  $Pt_{ex}$  atoms in the surface oxide phase, which is the main result of the structural analysis and the basis of the comparison with the DFT results, is a robust result and does not depend on the specific choice of the model employed in the CTR analysis.

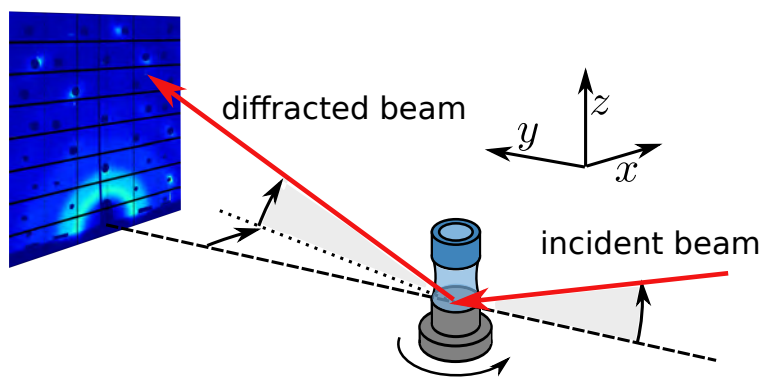
1.07 V	3 relaxed layers		4 relaxed layers	
	O <sub>ads</sub> included	O <sub>ads</sub> omitted	O <sub>ads</sub> included	O <sub>ads</sub> omitted
$\theta_{ex}/\text{ML}$	$0.213 \pm 0.008$	$0.208 \pm 0.008$	$0.230 \pm 0.006$	$0.223 \pm 0.006$
$d_{ex}/\text{\AA}$	$1.29 \pm 0.04$	$1.41 \pm 0.05$	$1.307 \pm 0.030$	$1.40 \pm 0.04$
$\chi_r^2$	1.98	2.07	1.24	1.32
1.12 V	3 relaxed layers		4 relaxed layers	
	O <sub>ads</sub> included	O <sub>ads</sub> omitted	O <sub>ads</sub> included	O <sub>ads</sub> omitted
$\theta_{ex}/\text{ML}$	$0.405 \pm 0.007$	$0.404 \pm 0.007$	$0.320 \pm 0.007$	$0.301 \pm 0.007$
$d_{ex}/\text{\AA}$	$1.409 \pm 0.014$	$1.409 \pm 0.016$	$1.297 \pm 0.023$	$1.322 \pm 0.010$
$\chi_r^2$	3.21	3.23	1.84	1.75
1.17 V	3 relaxed layers		4 relaxed layers	
	O <sub>ads</sub> included	O <sub>ads</sub> omitted	O <sub>ads</sub> included	O <sub>ads</sub> omitted
$\theta_{ex}/\text{ML}$	$0.5836 \pm 0.0008$	$0.577 \pm 0.006$	$0.5347 \pm 0.0012$	$0.5193 \pm 0.0010$
$d_{ex}/\text{\AA}$	$1.4070 \pm 0.0021$	$1.417 \pm 0.012$	$1.328 \pm 0.004$	$1.3385 \pm 0.0029$
$\chi_r^2$	3.18	3.52	2.00	2.20

**Supplementary Table 4.** Coverage  $\theta_{ex}$  and vertical position  $d_{ex}$  of the extracted Pt atoms obtained from CTR fits of the oxide structure at 1.07 V, 1.12 V and 1.17 V using 4 different oxide models. This allows an estimation of the systematic error due to the choice of the surface oxide model.

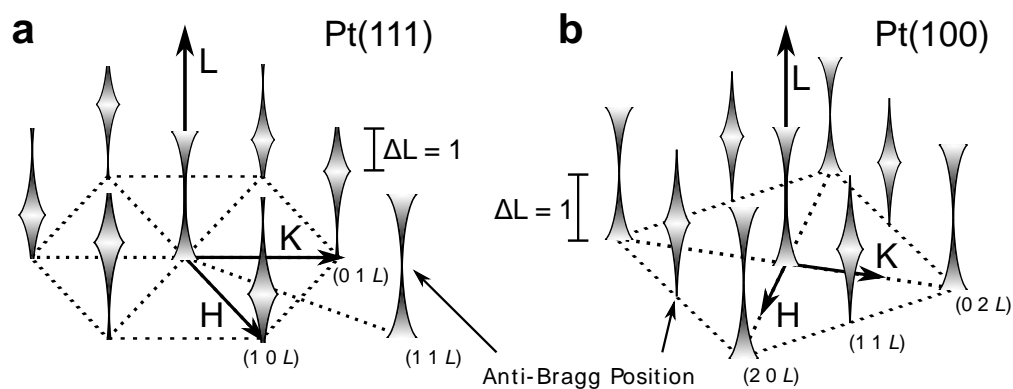




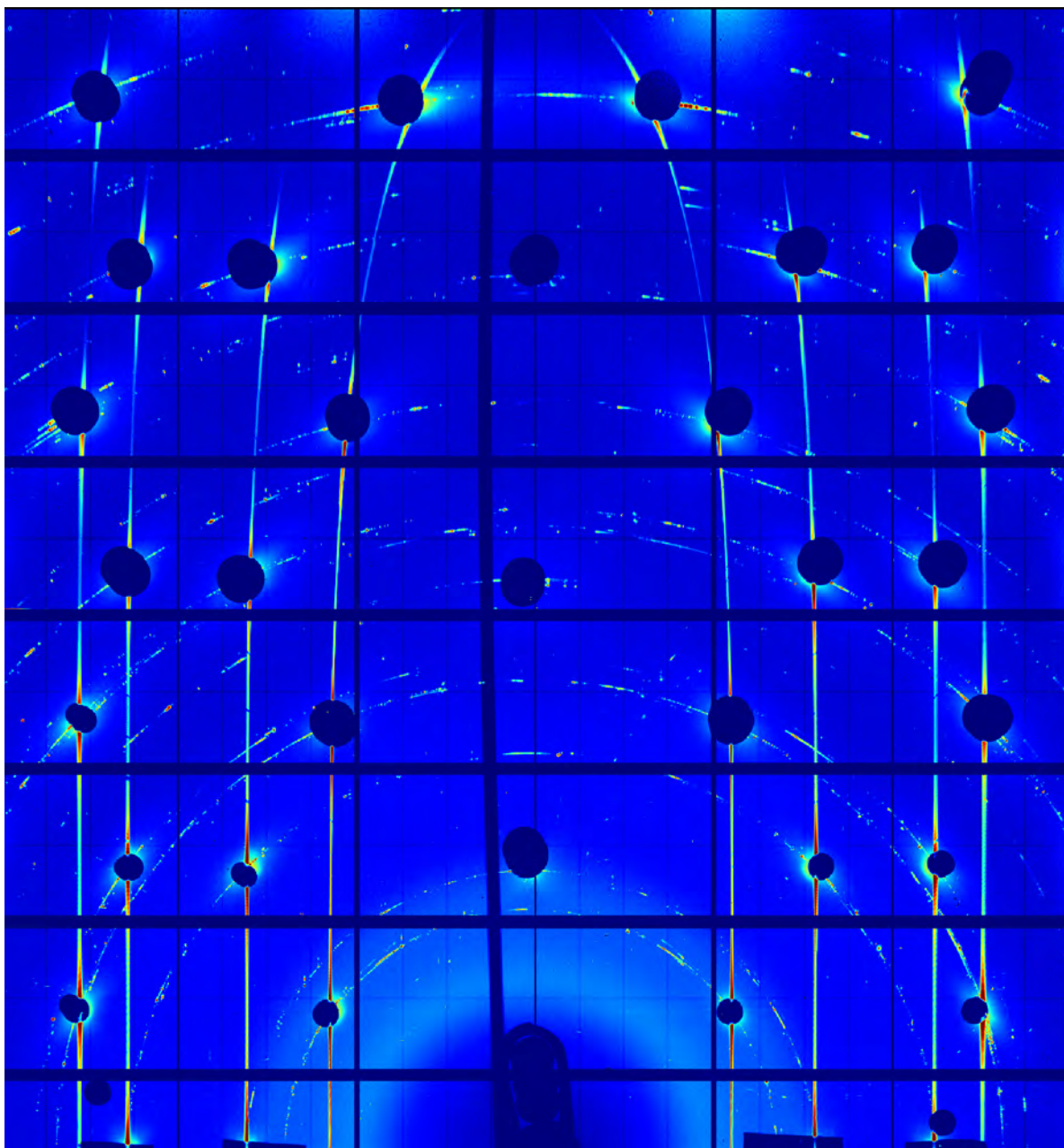
**Supplementary Figure 5.** (a): CTRs and corresponding fits at 0.95 V, and at 3 different potentials in the region of oxide formation using a surface model with adsorbed oxygen ( $O_{ads}$ , solid lines) or omitting  $O_{ads}$  (dashed lines). The grey line shows the fit of the smooth surface at 0.95 V. (b): Electron density obtained from the CTR fits.



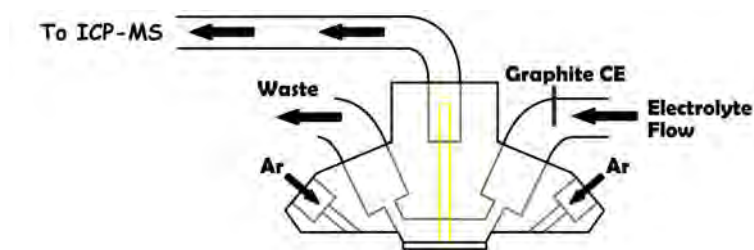
**Supplementary Figure 6.** Schematic illustration of the diffraction geometry, showing the incident and scattered X-ray beam (red).



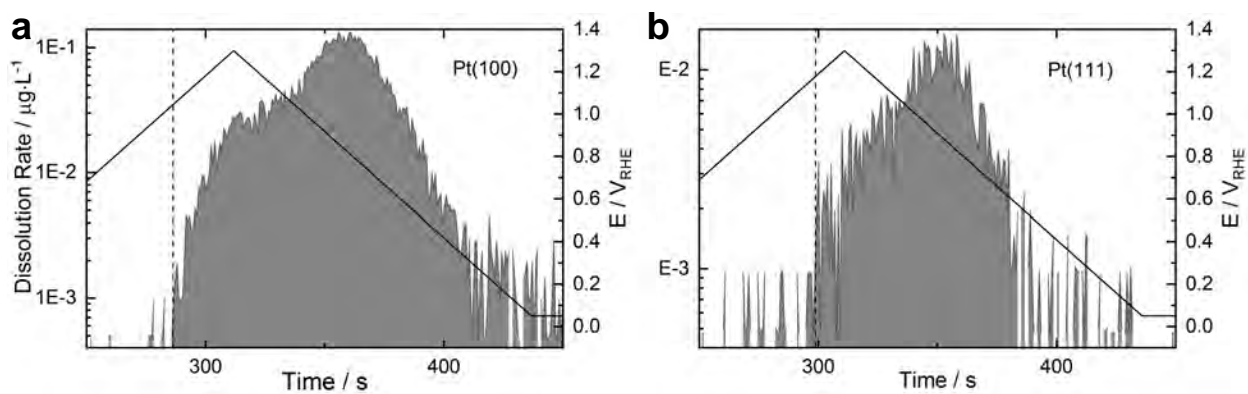
**Supplementary Figure 7.** Schematic illustration of the reciprocal space geometry for **(a)** Pt(111) and **(b)** Pt(100). The typical intensity distribution along the CTRs is indicated by the widths of the rods.



**Supplementary Figure 8.** Combination of all 2200 detector frames recorded during a reciprocal space mapping of Pt(100) at 0.12 V using HESXRD at ID31. The CTRs appear as vertical lines, which bend towards the center of the image in the upper part of the image due to the curvature of the Ewald sphere. In this representation, some symmetrically equivalent CTRs lie on top of each other. The black horizontal and vertical bars are insensitive parts of the detector; the black circles along the CTRs are beam stops, placed at the positions of Bragg reflections. The image has been normalized using a logarithmic scale.



**Supplementary Figure 9.** Scheme of CSFC-ICP-MS cell.



**Supplementary Figure 10.** Estimation of the onset potential of Pt dissolution on Pt(100) (a) and Pt(111) (b). A line was drawn from the visible onset of dissolution over the baseline to the corresponding potential (3 repeat experiments for each surface).

$\theta_{\text{O}}$	$\Delta G_{\text{O}}$ @ Pt(111)	$\Delta G_{\text{O}}$ @ Pt(100)	ZPE @ Pt(111)	TS <sub>vib</sub> @ Pt(111)	ZPE @ Pt(100)	TS <sub>vib</sub> @ Pt(100)
0.11	1.19	1.16	0.07	0.04	0.07	0.05
0.22	1.24	1.17	0.14	0.10	0.14	0.11
0.33	1.36	1.24	0.22	0.11	0.21	0.15
0.44	1.49	1.28	0.31	0.14	0.29	0.22
0.56	1.61	1.30	0.39	0.17	0.37	0.23
0.67	1.71	1.45	0.48	0.20	0.45	0.29
0.78	1.91	1.53	0.56	0.23	0.54	0.31
0.89	2.08	1.62	0.62	0.28	0.63	0.35
1.00	2.24	1.68	0.67	0.34	0.71	0.39

**Supplementary Table 5.** Average adsorption energies of oxygen (in eV/ $\text{O}_{\text{ads}}$ ) and zero-point energy (ZPE), and vibrational entropy (TS<sub>vib</sub>, at T = 298.15 K) corrections in eV for  $\text{O}_{\text{ads}}$  on Pt(111) and Pt(100).

species	ZPE	TS	$\Delta G_{\text{sol}}$
H <sub>2</sub> O	0.58	0.67	-
H <sub>2</sub> (g)	0.28	0.40	-
·H <sub>2</sub> O	0.64	0.18	-0.51

**Supplementary Table 6.** Zero-point energy (ZPE), entropy (TS, at T = 298.15 K) and solvation ( $G_{\text{sol}}$ ) corrections for various fluid-phase and adsorbed species. <sup>3</sup> All values are in eV.



## Supplementary References

1. Tidswell, I., Markovic, N. & Ross, P. Potential dependent surface structure of the Pt(1 1 1) electrolyte interface. *J. Electroanal. Chem.* **376**, 119 – 126 (1994).
2. Conway, B. E., Barnett, B., Angerstein-Kozłowska, H. & Tilak, B. V. A surface-electrochemical basis for the direct logarithmic growth law for initial stages of extension of anodic oxide films formed at noble metals. *J. Chem. Phys.* **93**, 8361–8373 (1990).
3. He, Z.-D., Hanselman, S., Chen, Y.-X., Koper, M. T. M. & Calle-Vallejo, F. Importance of Solvation for the Accurate Prediction of Oxygen Reduction Activities of Pt-Based Electrocatalysts. *J. Phys. Chem. Lett.* **8**, 2243–2246 (2017).